

# UltraFast Layer-Resolved Encoding (uFLARE) functional MRI deciphers bidirectional signaling from spontaneous activity

Received: 23 March 2025

Accepted: 17 March 2026

Published online: 04 May 2026

 Check for updates

Joana Carvalho <sup>1,2</sup> ✉, Francisca F. Fernandes <sup>1</sup>, Mafalda Valente <sup>1</sup>,  
Koen V. Haak <sup>3,4</sup> & Noam Shemesh <sup>1,5</sup> ✉

Deciphering the directionality of information flow in cortical circuits is essential for understanding brain dynamics, learning, and neuroplasticity after injury. However, current noninvasive methods cannot distinguish bottom-up from top-down signals across entire networks, including deep brain regions. Here, we present UltraFast Layer-Resolved Encoding (uFLARE) that combines ultrafast-fMRI with a Layer-based Connective Field (ICF) model to disentangle bottom-up from top-down signaling. Our findings reveal that ICF size, an indicator of information integration, differentiates bottom-up and top-down activity through distinct layer-specific connectivity patterns during spontaneous activity, challenging the previous suggestions that bottom-up signals are solely stimulus-driven. Bottom-up connectivity follows an inverted U-shape, peaking in layer IV, while top-down exhibits a U-shaped pattern, with peaks in layers I and VI. These profiles generalize across sensory pathways (visual, somatosensory, and motor) and reveal injury-induced network reorganization, such as LGN bypassing V1 to provide direct bottom-up input to higher visual areas.

Sensory processing depends on hierarchical and reciprocal communication across brain regions<sup>1–4</sup>, with signals flowing dynamically between early sensory areas and higher cortical areas<sup>5–7</sup> in multiple species<sup>8,9</sup>. This bidirectional information flow allows early sensory areas to relay encoded sensory information to higher cortical regions for further processing, which is then fed back to refine or modulate the initial processing in the early regions<sup>10–12</sup>. Bottom-up processing begins with the capture of sensory input, followed by a feedforward sweep in which neural activity elicited by the stimulus propagates from low-level sensory areas to higher-order regions. In this process, simple receptive fields in primary sensory areas are gradually combined into more complex representations in higher cortical areas<sup>2</sup>. In contrast, top-down processing involves feedback from higher-order areas that

modulate activity in lower sensory regions, integrating factors such as attention<sup>12,13</sup>, prediction<sup>14</sup>, and contextual cues to shape perception in a meaningful, adaptive way<sup>15</sup>. Differentiating the directionality of information flow in cortical circuits is key to understanding neural computations underlying learning, perception, and neuroplasticity<sup>16–19</sup>. However, dissociating bottom-up from top-down signals remains challenging due to their concurrence and their distribution in wide networks in the brain. So far, studying bottom-up and top-down signals has relied on invasive methods like electrophysiology, calcium imaging, photometry<sup>20</sup>, and optogenetics, which provide high specificity but are limited to subsets of neurons, potentially missing pathway-wide mechanisms<sup>2,21–23</sup>. In humans, electrocorticography has been used but remains invasive and localized<sup>11</sup>. Noninvasive

<sup>1</sup>Champalimaud Research, Champalimaud Foundation, Lisbon, Portugal. <sup>2</sup>Visual Neuroscience Laboratory, Faculty of Psychology and Educational Sciences, University of Coimbra, Coimbra, Portugal. <sup>3</sup>Department of Intelligent Systems, Research Center for Cognitive Science and Artificial Intelligence, Tilburg School of Humanities and Digital Sciences, Tilburg University, Tilburg, The Netherlands. <sup>4</sup>Donders Institute for Brain, Cognition and Behaviour, Centre for Cognitive Neuroimaging, Radboud University, Nijmegen, The Netherlands. <sup>5</sup>Chemical and Biological Physics, Weizmann Institute of Science, Rehovot, Israel. ✉ e-mail: [joana.carvalho@fpce.uc.pt](mailto:joana.carvalho@fpce.uc.pt); [Noam.Shemesh@neuro.fchampalimaud.org](mailto:Noam.Shemesh@neuro.fchampalimaud.org)

techniques like MEG and EEG offer good temporal resolution but lack the spatial precision and depth required to investigate local circuits, such as those within cortical columns<sup>24,25</sup>, or more broadly distributed systems. Additionally, signal overlap from neighboring areas complicates bottom-up and top-down segregation in these techniques.

Functional MRI provides a critical view into brain-wide signal processing<sup>26–28</sup>. Ultrahigh-field MRI provides noninvasive access to high spatial resolution<sup>29,30</sup> and can enable the segregation of cortical layer signals through neurovascular coupling<sup>31–33</sup>, offering insights into bottom-up and top-down processing<sup>29,34–36</sup>. Previous research has often relied on manipulating experimental paradigms to isolate bottom-up and top-down signals, such as occlusion paradigms<sup>37</sup>, visual illusions<sup>38</sup>, attentional tasks<sup>39</sup> and contrasting visual perception with imagery<sup>40</sup>. Bottom-up and top-down signals can be distinguished based on their cortical layer of origin and reception<sup>41</sup>. Bottom-up signals typically originate in middle cortical layers<sup>42</sup>, while top-down signals show variability, arriving in deep<sup>43,44</sup>, superficial<sup>37,42</sup>, or both layers<sup>45,46</sup>. Despite these advances, noninvasively distinguishing bottom-up from top-down signals from spontaneous activity has not been achieved, due to their spatiotemporal overlap.

The temporal dynamics of bottom-up and top-down signals have received relatively limited attention in fMRI due to the limited resolution of conventional methods and the slow and variable hemodynamic coupling. Notably, bottom-up and top-down signals exhibit distinct temporal characteristics: bottom-up activity operates at higher frequencies (30–50 Hz) and occurs shortly after stimulus onset, while top-down is slower (3–6 Hz)<sup>6</sup> and more prevalent during spontaneous activity, making their interaction with neurovascular coupling interesting to target<sup>47</sup>. Advances in preclinical high-field MRI now allow sub-millimeter resolution (~150  $\mu\text{m}$ ) and rapid sampling (~30–50 ms)<sup>48–50</sup>, enabling the accurate mapping of stimulus-evoked neural input<sup>49,51</sup>. Critical developments in ultrafast fMRI acquisitions, first via line scanning<sup>52–54</sup>, and more recently through 2D imaging<sup>49,51</sup>, revealed fine structure in BOLD signals<sup>55</sup>. A recent ultrafast resting-state (RS) fMRI study highlighted the wealth of information embedded in spontaneous signals, revealing oscillations that drive long-range connectivity<sup>50</sup> with neuronal origins<sup>56,57</sup>.

Here, we present UltraFast Layer-Resolved Encoding (uFLARE) that captures the distinct spatiotemporal characteristics of bottom-up and top-down signals. To model bottom-up and top-down signals, an effective bidirectional computational model is essential. uFLARE evolves from the connective field (CF) modeling<sup>58–61</sup>—which unlike conventional functional connectivity (FC)—can capture directional specificity by leveraging CF size as a measure of spatial pooling, which varies across cortical layers. This unique bidirectionality allows CF modeling to resolve bottom-up and top-down information flow, even during RS activity, where both signals are more balanced than during stimulation. While prior CF applications have been limited to connectivity between cortical areas via bottom-up processing and could not differentiate bottom-up from top-down sources<sup>61–63</sup>, we here developed uFLARE: an ultrahigh spatiotemporal resolution fMRI approach combined with a layer-specific CF (ICF) model for characterizing the directionality of information flow between cortical layers (Fig. 1). The ensuing uFLARE-fMRI approach enables, for the first time, the prediction of neural activity in a specific voxel based on aggregate information from the layer it samples or to which it sends information. Noninvasive and network-wide in scope, uFLARE uniquely dissociates source and target layers, offering the ability to reveal specific bottom-up and top-down patterns noninvasively with fMRI, both in task-based and in RS activity.

## Results

We developed the uFLARE framework to resolve bottom-up and top-down information. Our work is presented in the following structure: first, we applied uFLARE to investigate information flow in the rat

visual pathway. We investigated area-to-layer projections from precortical areas to the primary visual cortex (V1), demonstrating the accuracy of the model in unraveling which layers receive bottom-up signals from subcortical areas (Section “Area-to-layer connective fields reveal the bottom-up flow of information in the geniculate and extrageniculate pathways”). Next, we examined layer-to-layer communication between primary and higher cortical areas (Section “Layer-to-layer connective fields across cortical depth resolve top-down and bottom-up signals in spontaneous activity”), revealing unique signatures for both bottom-up and top-down signals across cortical areas. We then demonstrated that our findings in the visual system generalize to other cortical areas (Section “uFLARE reveals directional connectivity in the somatosensory and motor cortices”), and analyze where the specificity comes from (Section “Higher number of samples in uFLARE improves top-down / bottom-up discrimination”). Finally, we applied our ICF approach to assess plasticity following network perturbations (Section “uFLARE reveals circuit reorganization following cortical lesions”).

### Area-to-layer connective fields reveal the bottom-up flow of information in the geniculate and extrageniculate pathways

We first examine bottom-up and top-down signaling in the rodent visual system, which consists of two main pathways: the geniculate pathway, where V1 receives direct input from the lateral geniculate nucleus (LGN), primarily targeting layer IV (LIV), and the extrageniculate pathway, where the lateral posterior nucleus (LP) projects to higher visual areas (HVA) in LIV and LV (Fig. 2A). To assess whether fMRI can capture these pathways, we conducted multislice acquisitions of the visual system during RS, and applied the ICF model to quantify projections from LGN and LP to different visual cortex (VC) layers. The CF model predicts activity in one region (e.g., V1 layers) based on the aggregate activity in another region (e.g., LGN), typically using a Gaussian kernel (Fig. 1) to weight and integrate the time series, creating a predicted target signal. The center of the CF represents the location in brain space that has the highest correlation with the target area, while the size of the CF indicates the extent of information integration. CF models have been shown to capture topographically specific BOLD responses<sup>61,62</sup>. Figure 2C, D illustrates the CF polar maps obtained by projecting retinotopic coordinates, measured in a separate scanning session where retinotopic mapping was performed, onto the CF locations ( $\nu_0$ ). The CF polar angle reveals a structured, retinotopic pattern across the entire visual pathway when the source is defined as either LGN or LP. The retinotopic pattern obtained from CF is very similar to the one obtained from retinotopic mapping (Fig. S1). Notably, in the VC, the phase reversal points of the CF polar angle align with the borders between visual areas. This finding suggests that, even in the absence of direct visual input, functional connectivity preserves a visuotopic organization.

Figure 2E, F shows distinct projection patterns from the LGN and LP to different areas and layers of the VC, highlighting specialized pathways for visual information processing. When examining projections from the LGN to V1, we observed that the largest cortical CF sizes are concentrated in the middle layers, particularly layer IV, as shown in Fig. 2E. This finding is further quantified in Fig. 2G, which demonstrates an inverted U-shaped profile of CF sizes, peaking in layer IV and decreasing in both the superficial and deeper layers. This characteristic profile suggests that LGN inputs are precisely targeted to the middle layers of V1. Notably, this inverted U-shape pattern is absent in the LGN projections to HVA, indicating a more specialized and layer-specific role for LGN inputs in V1. In contrast, LP projections show a complementary pattern. LP primarily feeds information to HVA rather than V1. In the secondary visual cortex (V2), the LP projections exhibit an inverted U-shaped CF profile, similar to the LGN to V1 pattern, peaking in the middle layers (Fig. 2H). LP projections to V1, as well as LGN projections to V2, display a linear increase in CF size with cortical depth. A one-way ANOVA analysis of the quadratic coefficients of the

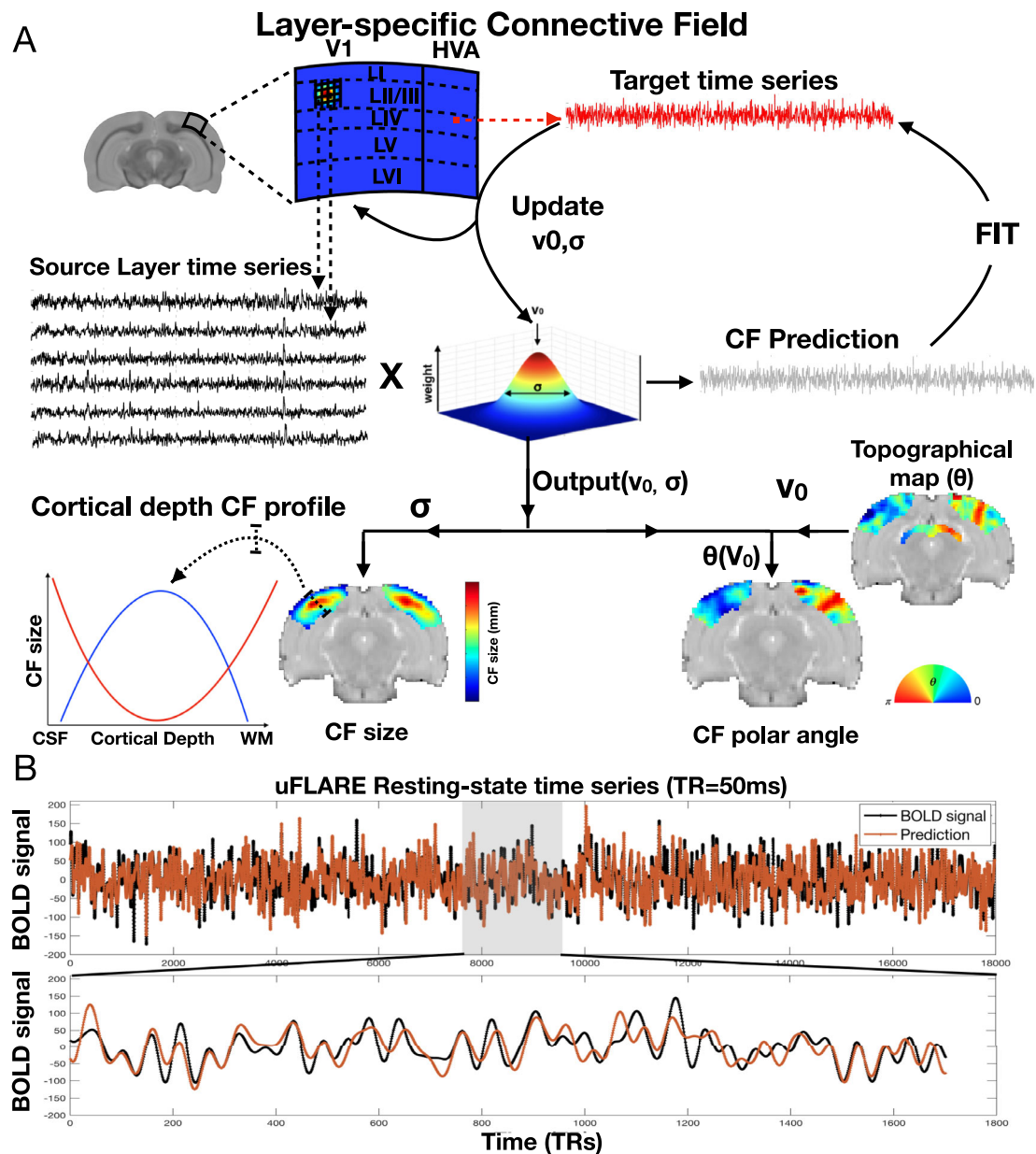


**Fig. 1 | Scheme of the Layer CF model applied to ultrafast fMRI data. A:** The ICF model predicts the neural activity of a recording site (voxel) in a target layer (e.g., layer IV of higher visual order areas (HVA)) based on the aggregate activity of a source layer or region (e.g., layer II/III of V1). Each voxel's fMRI response is predicted using a 2D circular Gaussian CF model. The output parameters of the CF model are its center position ( $v_0$ ) in brain space and size ( $\sigma$ ) within the source cortical layers. With a defined CF position and size, a predicted time-series is generated by weighting the CF model with the source BOLD time series. Optimal CF parameters

are determined by minimizing the residual sum of squares between the predicted and actual time-series data. Our hypothesis was that, since ICF size reflects the extent of information integration, it would vary across cortical depth (layers). Specifically, we expected bottom-up connections to exhibit an inverted U-shaped pattern, given that visual input is primarily processed in layer IV (LIV), while top-down connections would follow a U-shaped pattern. **B:** Example trace of time series measured (black) and predicted (red) of an HVA voxel of layer IV based on aggregate activity from V1 LII/III.

functions describing CF size profiles across cortical depth revealed that the coefficients for LGN  $\rightarrow$  V1 significantly differ from those for LGN  $\rightarrow$  HVA ( $F(1,10) = 18.87$ ,  $p = 0.0015$ ), as well as LP  $\rightarrow$  HVA differed from LP  $\rightarrow$  V1 ( $F(1,10) = 14.68$ ,  $p = 0.003$ ) (Fig. 2I). However, no significant differences were observed between LP  $\rightarrow$  HVA and LGN  $\rightarrow$  V1, nor between LP  $\rightarrow$  V1 and LGN  $\rightarrow$  HVA. Furthermore, the quadratic coefficients obtained for LGN  $\rightarrow$  V1 and LP  $\rightarrow$  HVA were statistically different from 0 (LGN  $\rightarrow$  V1  $t(5) = 5.6$ ,  $p = 0.003$ ,  $d = 2.29$ ; LP  $\rightarrow$  HVA  $t(5) = -17.7$ ,  $p = 1 \times 10^{-5}$ ,  $d = -7.22$ ), while the coefficients obtained for LGN  $\rightarrow$  HVA ( $t(5) = -0.06$ ,  $p = 0.95$ ,  $d = -0.02$ ) and LP  $\rightarrow$  V1 ( $t(5) = -1.7$ ,  $p = 0.16$ ,  $d = -0.69$ ) were not significantly different from zero. The

inverted-U and U-shaped correlation patterns were consistently observed in both hemispheres and are uniform within one visual area. Our findings indicate that the layer-specific CF profiles across cortical depth are primarily shaped by layer-dependent input and output connectivity, rather than by polar angle organization. Note that the CF size is independent of the population receptive field size. The pRF sizes are larger in HVAs (Fig. S1), and in V1 pRFs tend to be larger in superficial and deeper layers than in the middle layer (Fig. S1<sup>45</sup>).

Importantly, high temporal resolution also improves the accuracy of the CF estimation. Figure S6 demonstrates that the variance explained (VE) of the ICF model when applied to ultrafast data has an

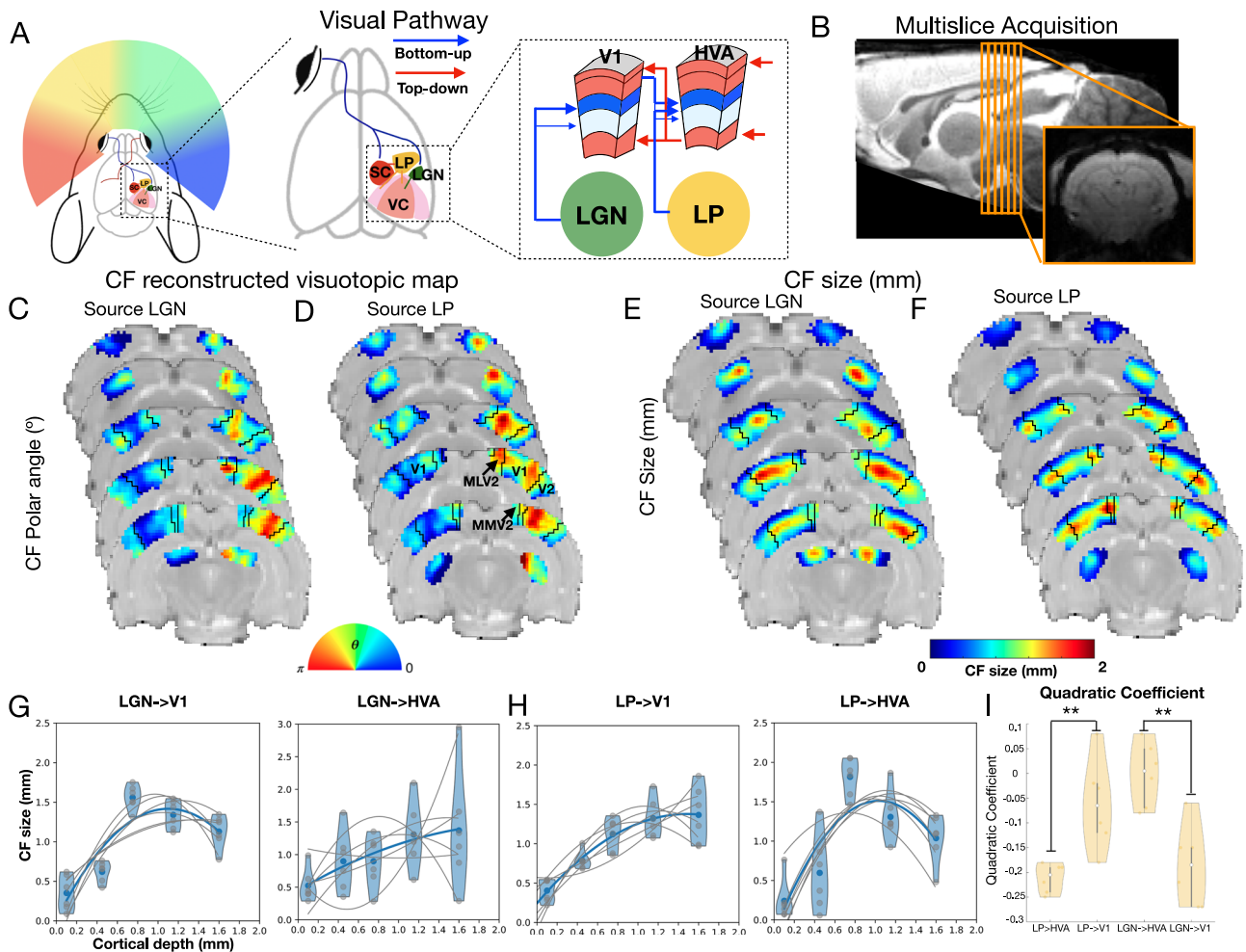


**Fig. 2 | Area-to-layer CF profiles obtained for bottom-up projections.** **A** Schematic illustration of the visual pathway, highlighting primary structures involved in bottom-up and top-down connections. The mouse drawing is adapted from Petrucco, L. *Mouse head schema* (2020), Zenodo (<https://doi.org/10.5281/zenodo.3925903>), licensed under CC BY 4.0. **B** Slices acquired in the multislice ultrafast RS fMRI datasets and a representative functional slice. Visualizations of CF polar angle (**C, D**) and CF size (**E, F**) averaged across participants projected onto brain slices, with LGN (**C, E**) and LP (**D, F**) serving as the source areas. Black lines define the boundaries of VC areas. **G, H** CF size profile (normalized to the mean) across the cortical layers of V1 and higher visual order areas (HVA), in particular, Secondary Visual Cortex (V2), Medio Lateral Secondary Visual Cortex (MLV2),

Medio Medial Secondary Visual Cortex (MMV2). The CF models were performed with LGN and LP serving as the source areas, respectively. The gray dots represent the data from each individual animal, and the gray lines represent the parabolic fit per animal. The blue dots and lines represent the median of all animals. **I** Quadratic Coefficients obtained for the ICF size profile across cortical layers. The yellow dots represent the quadratic coefficient from each individual animal ( $n = 6$ ). The white dot represents the median and the gray line the 1st and 3rd quartiles. The \*\*\* represents a  $p$  value  $< 0.001$ , \*\*  $p$  value  $< 0.01$ , and \*  $p$  value  $< 0.05$ , from the two-sided  $t$ -test: LGN  $\rightarrow$  V1 ( $t(5) = 5.6, p = 0.003, d = 2.29$ ); LP  $\rightarrow$  HVA ( $t(5) = -17.7, p = 1 \times 10^{-5}, d = -7.22$ ); LGN  $\rightarrow$  HVA ( $t(5) = -0.06, p = 0.95, d = -0.02$ ) and LP  $\rightarrow$  V1 ( $t(5) = -1.7, p = 0.16, d = -0.69$ ). Source Data has been included as a Source Data file.

increase two-to-four fold compared with standard temporal resolution fMRI data.

Brain connectivity is typically analyzed using FC, which, unlike CF, does not account for spatial pooling between brain regions. As a result, FC has traditionally been considered unidirectional, as it reflects correlations between voxels or brain areas. However, FC strength could, in principle, help distinguish between bottom-up and top-down pathways based on characteristic FC strength profiles across cortical layers. For instance, if FC strength between LGN and V1 peaks in the middle layers of V1, this may indicate bottom-up signaling. To assess whether the inverted U-shaped, layer-specific CF profile—which reflects bottom-up signaling—can be inferred from conventional FC methods, we computed the FC between the LGN, SC, LP, and V1 layers (Fig. S2A and Table S1). The FC profile across cortical depth for all three connections (LGN, SC, and LP to V1 layers) did show an inverted U-shaped trend, with the highest correlation coefficients observed in the middle V1 layers. However, the data exhibited high variability, resulting in very

shallow parabolic coefficients (LGN  $\rightarrow$  V1:  $-0.02$ ; LP  $\rightarrow$  V1:  $-0.01$ ; SC  $\rightarrow$  V1:  $-0.01$ ), and none were significantly different from zero (LGN  $\rightarrow$  V1:  $t(5) = -2.13, p = 0.08, d = -0.87$ ; LP  $\rightarrow$  V1:  $t(5) = -0.67, p = 0.53, d = -0.27$ ; SC  $\rightarrow$  V1:  $t(5) = -1.16, p = 0.3, d = -0.47$ ). Additionally, there were no significant differences in the parabolic coefficients among the LGN  $\rightarrow$  V1, LP  $\rightarrow$  V1, and SC  $\rightarrow$  V1 pathways ( $F(2,17) = 0.86, p = 0.44, d = 0.32$ ). In contrast, a comparison of the parabolic coefficients between the ICF size profile (Table S2) and FC profiles (Table S1) revealed a strong and highly significant difference ( $F(1,11) = 21.85, p = 0.0009, d = 1.41$ ). The parabolic curve associated with the ICF size profile was much more pronounced, with average parabolic coefficients of  $-0.19$  for LGN  $\rightarrow$  V1 and  $-0.21$  for LP  $\rightarrow$  HVA.

Another way to assess FC is through coherence, where higher coherence is generally interpreted as stronger FC<sup>64,65</sup>. We performed a coherence analysis between subcortical areas (LGN and LP) and V1 and V2 layers to understand which frequencies might be associated with bottom-up and top-down signals. The coherence analysis revealed

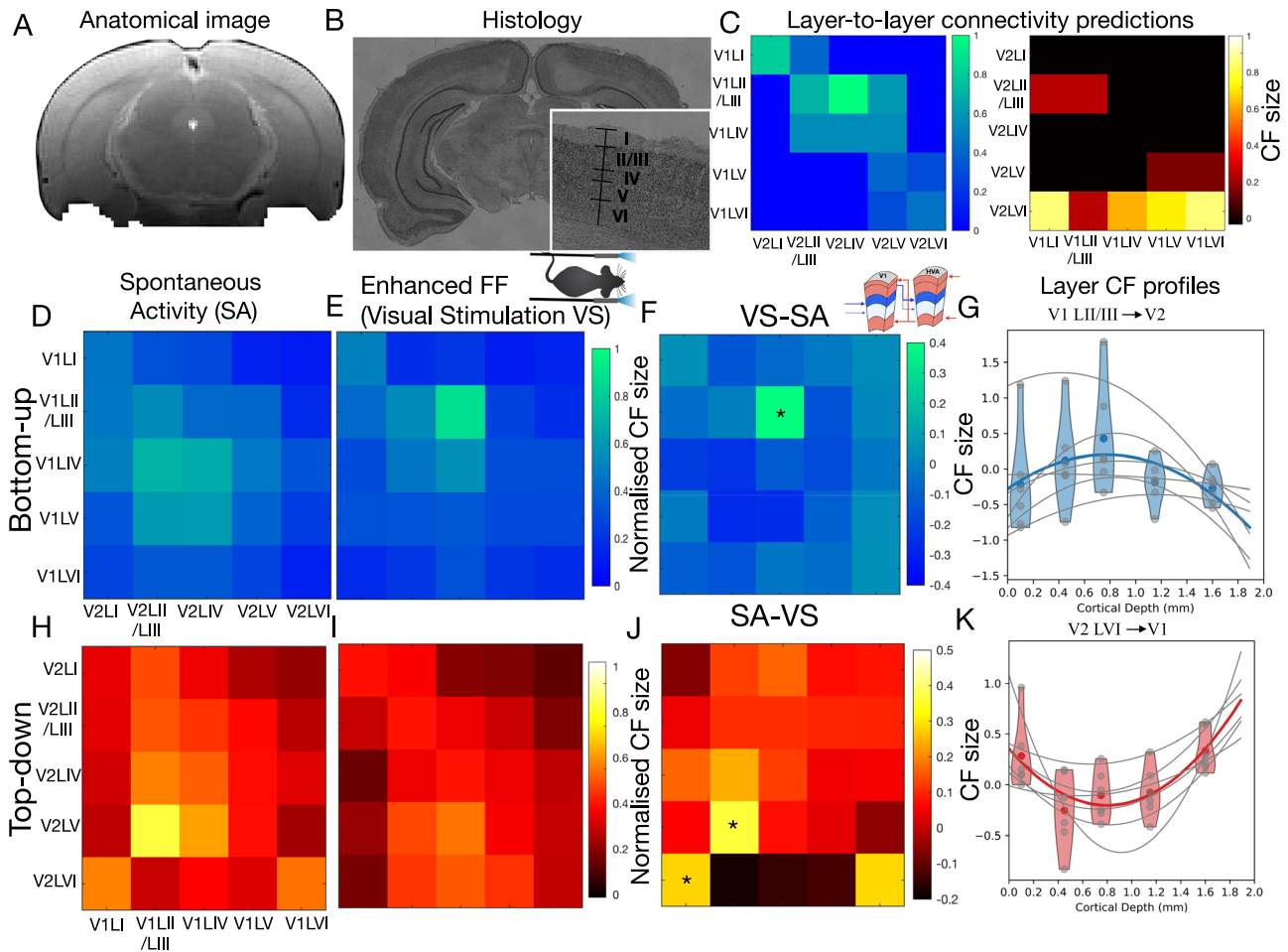


**Fig. 3 | Layer-to-layer CF profiles.** **A** High-resolution anatomical image. **B** A histological view delineating cortical layers. **C** Schematic representation of the expected layer-to-layer connections based on the literature. Bottom-up connections (V1 → V2) are indicated in the blue matrix and top-down connections (V2 → V1) are shown in a red/yellow scale (Federer et al.<sup>67</sup>). Bottom-up connectivity maps averaged across animals from V1 to V2 layers obtained under spontaneous activity (**D**) and visual stimulation (**E**), as well as the difference map subtracting spontaneous activity from visual stimulation non-normalized data, thereby isolating bottom-up-specific pathways (**F**). The mouse drawing is adapted from Costa, G. *Mouse Top* (2020), Zenodo (<https://doi.org/10.5281/zenodo.3926105>), licensed under CC BY 4.0. **G** The CF size profile (normalized to the mean) illustrates how V1 layer II/III projects across all cortical layers in V2. The gray dots represent the data from each individual animal, and the gray lines represent the parabolic fit per

animal. The blue dots and lines represent the median of all animals. Top-down connections averaged across participants between V2 to V1 layers acquired under spontaneous activity (**H**) and visual stimulation (**I**) conditions, with the visual stimulation data subtracted from RS data to isolate top-down-specific pathways (**J**). The subtraction was performed using the non-normalized maps. **K** The CF size profile (normalized to the mean) demonstrates projections from V2 layer VI to all V1 cortical layers. The gray dots represent the data from each individual animal, and the gray lines represent the parabolic fit per animal. The red dots and lines represent the median of all animals. For **F** and **J**, the \* represents statistically significant differences between visual evoked and spontaneous activity, resulting from a one-way ANOVA test with post hoc analysis Bonferroni corrected for multiple comparisons. Source Data has been included as a Source Data file.

laminar-specific connectivity profiles that closely resembled those captured by the CF size. Figures S3 and S4 show that direct bottom-up connections, such as LGN → V1 and LP → HVA, exhibit increased coherence in the middle layers, particularly at 0.025–0.03 Hz and 0.15 Hz. In contrast, non-direct connections (LGN → HVA and LP → V1) do not show this middle-layer coherence enhancement at these frequency ranges. Across all examined connections, we consistently observed coherence peaks in layers I and IV around 0.17–0.18 Hz. Although the origin of these peaks remains unclear, they appear biologically driven and may reflect propagating waves of activity (see Supplementary Video S1).

To further investigate the impact of the frequency bands on the detection of bottom-up and top-down signals, we repeated the area-to-layer analysis using three different band pass (BP) filters: 0.01–0.1 Hz, 0.01–0.2 Hz, and 0.01–0.4 Hz. Figure S5 shows the area-to-layer CF size profiles obtained for the connections LGN → V1, LGN → HVA, LP → V1, and LP → HVA across these frequency intervals. With the narrowest BP

filter (0.01–0.1 Hz), the inverted U-shaped CF size profiles across cortical depth for the direct bottom-up connections (LGN → V1 and LP → V2) are relatively shallow. Including higher-frequency bands sharpens these profiles, producing clearer parabolic shapes with higher parabolic coefficients (see Fig. S5), the strongest being in the 0.01–0.4 Hz range. This suggests that relevant information exists in broader-frequency bands, at least beyond the 0.01–0.1 Hz range typically used in RS fMRI analyses.

**Layer-to-layer connective fields across cortical depth resolve top-down and bottom-up signals in spontaneous activity**

Using single-slice acquisitions with an ultrahigh spatiotemporal resolution (164 μm × 165 μm) at 55 ms during spontaneous activity (where top-down signals are enhanced and top-down > bottom-up<sup>66</sup>) and continuous binocular visual stimulation (bottom-up enhanced, bottom-up > top-down<sup>22</sup>), we computed layer-to-layer CFs between V1 and V2 layers (Fig. 3D–K). Layer-to-layer CF sizes revealed two distinct

connectivity profiles across cortical layers that align with layer-specific bottom-up and top-down patterns: V1 projects to the middle layers of V2 (inverted-U-shaped profile), while the deep layers of V2 predominantly relay top-down signals to the superficial and deep layers of V1 (U-shaped profile, Fig. 3G, K).

In the context of bottom-up projections from V1 to V2, we observed distinct ICF patterns between spontaneous and visual stimulation conditions. During spontaneous activity, the most prominent connections—characterized by a large pooling extent (large ICF sizes)—were from V1 layer IV to V2 LII/III and LIV (Fig. 3D). Under visual stimulation, the large ICF sizes were measured from V1 LII/LIII to V2 LII/LIII and LIV, and from V1 LIV to V2 LIV (Fig. 3E). To differentiate the specific effects of bottom-up and top-down, we subtracted the spontaneous connectivity ICF size maps from those obtained during visual stimulation (Fig. 3F). This subtraction revealed pronounced connections between V1 LI and V2 LI, as well as between V1 LII/LIII and V2 LIV. The ICF size obtained for the projection of V1 LII/LIII to V2 LIV was significantly larger during visual stimulation than during spontaneous activity ( $F(1,11) = 8.92$ ,  $p = 0.0136$ ,  $d = 0.9$ ). Quantifying these connections showed that the CF sizes from V1 LII/III to all V2 layers exhibit an inverted U-shaped pattern, with the largest sizes in V2 layer IV (Fig. 3G).

For top-down connections from V2 to V1, spontaneous activity data showed strong projections (characterized by larger CF sizes) from V2 LV to V1 LI and LVI, and from V2 layer V to V1 LII/III and LIV (Fig. 3H). By subtracting the visual stimulation ICF size maps from the spontaneous activity maps, we identified stronger sampling (larger CF sizes) between V2 layer VI and V1 LI ( $F(1,11) = 6.99$ ,  $p = 0.02$ ,  $d = 1.53$ ) and VI ( $F(1,11) = 4.25$ ,  $p = 0.06$ ,  $d = 1.19$ ), and between V2 layer V and V1 LII/III ( $F(1,11) = 9.18$ ,  $p = 0.01$ ,  $d = 1.75$ ) (Fig. 3J). This was further quantified by analyzing the CF size profile across cortical depth from V2 LVI to all V1 layers, which exhibited a U-shaped profile, with CF sizes peaking in V1 LI and LVI (Fig. 3K). In a separate experiment, we applied the ICF model to a 45 s OFF/15 s ON stimulation paradigm, with the same acquisition parameters as before (TR = 55 ms), Fig. S12. Our connectivity analysis (Fig. S12C–F) shows similar patterns to the continuous visual stimulation Fig. 3E, I, with the bottom-up connections (V1 → HVA) exhibiting inverse U-shaped CF size profiles across cortical depth, while the top-down connections do not display the typical U-shaped profile. These results can be explained by (1) the substantially stronger feedforward responses upon receiving the stimulus; (2) the higher correlation between time series across visual areas and cortical layers affects the performance of the CF model; (3) the sedation may further reduce top-down control following the input<sup>22</sup>.

The layer-to-layer bottom-up and top-down connectivity maps, obtained with high spatiotemporal resolution, exhibit patterns similar to those derived from high temporal resolution (50 ms) and standard spatial resolution during spontaneous activity (Fig. S7). Notably, these maps were acquired from different animals and scanning sessions, demonstrating the reproducibility of the ICF model. Additionally, Fig. S7 presents bottom-up and top-down connectivity maps HVA, both of which demonstrate comparable connectivity profiles: bottom-up predominantly links middle layers, while top-down primarily targets deeper layers.

Importantly, the layer-to-layer connectivity profiles obtained using ICF align with the projections identified in electrophysiology and calcium imaging studies using retrograde viral tracing and post-mortem quantification of axonal projections<sup>67–69</sup>, as shown in Fig. 3C. Figure 3C shows a strong bottom-up projection between V1 LII/LIII and V2 LIV, and a strong top-down projection between V2 LVI and V1 LI and LIV.

FC strength is typically calculated using Pearson correlations, meaning that layer-to-layer FC between V1 and V2 is symmetrical (i.e.,  $FC(V1 \rightarrow V2)$  is indistinguishable from  $FC(V2 \rightarrow V1)$ ). As a result, this approach cannot disentangle the direction of information flow. Figure S2B illustrates the layer-specific FC calculated between V1 and V2

layers, revealing that the FC map  $V2 \rightarrow V1$  is symmetrical to  $FC V2 \rightarrow V1$  and that FC profiles differ substantially from those obtained using the ICF model both for the bottom-up connections ( $V1LV \rightarrow V2LIV$ ,  $V1LV \rightarrow V2LV$ ,  $V1LVI \rightarrow V2LIV$ ,  $V1LVI \rightarrow V2LV$ ) as well as for top-down connections ( $V2LII/III \rightarrow V1LVI$ ,  $V2LIV \rightarrow V1LV$ ,  $V2LIV \rightarrow V1LVI$ ,  $V2LV \rightarrow V1LII/III$ ,  $V2LV \rightarrow V1LV$ ,  $V2LV \rightarrow V1LVI$ ;  $V2LVI \rightarrow V1LI$ ,  $V2LVI \rightarrow V1LVI$ ).

We also examined the coherence between V1 and V2 layer-to-layer connections; Fig. S3B shows that the strongest coherence is observed between the middle layers of V1 and V2, consistent with the flow of bottom-up information from V1 into V2 input layers (LII/III and LIV). In contrast, the reverse direction ( $V2 \rightarrow V1$ ) shows weaker coherence overall, although relatively higher values are detected between V2 and the deep layers of V1 (LVI). Similar to the area-to-layer analysis, the  $V1 \rightarrow V2$  layer-to-layer coherence also shows frequency-specific increases at 0.025–0.03 Hz and 0.15 Hz, supporting the interpretation of frequency-dependent bottom-up interactions. Both coherence and CF metrics reflect cortical connectivity and information flow. Importantly, by extending the frequency range beyond the standard 0.1 Hz cutoff typically used in RS fMRI, we capture additional information about both bottom-up and top-down signals.

### UFLARE reveals directional connectivity in the somatosensory and motor cortices

To investigate whether the CF size profiles for bottom-up and top-down pathways observed in the visual system are general (i.e., they exhibit similar properties in other brain regions), we analyzed area-to-layer and layer-to-layer CFs in the somatosensory and motor pathways from multislice and single-slice ultrafast data, respectively. Given that the cortex in somatosensory and motor areas is thicker than in the VC, we were able to define cortical layers with greater precision using standard spatial resolution data (Fig. 4B).

In both the primary somatosensory cortex (SM1) and primary motor cortex (M1), layer IV receives direct input from thalamic structures, such as the ventral posterolateral nucleus (VPL) (Fig. 4A). When VPL was set as the source, CF size profiles showed larger values in layer IV of SM1, with an inverted U-shaped profile that peaked at this layer (Fig. 4D, E), consistent with findings in the visual pathway (Fig. 2E–H). Additionally, SM1 and M1 exhibit strong connectivity through LII/III and LV (Fig. 4A). When examining the CF size profiles across these layers, we observed slightly larger CF sizes in LII/III and LV than in LI, LIV and LVI (Fig. 4D, E). The CF size profile between the secondary motor cortex (M2) and M1, despite mostly carrying top-down signals, also displayed an inverted U-shaped profile on average, although with a shallow curvature and high variability between animals.

The layer-to-layer connections between M1 and M2 (Fig. 4F) mirror those observed in the visual pathway, with deep layers of M1 projecting predominantly to the middle layers of M2. Quantification of CF size from M1 LVI to all M2 layers reveals an inverted U-shaped profile, with CF size peaking in LII/III and IV of M2 (Fig. 4G). Conversely, the connections from M2 to M1 show the opposite pattern: the deep layers of M2 (LV and LVI) feed information to the superficial layers of M1 (LI and LII/III), while the middle layers of M2 (LII/III, LIV, and LV) project to the deep layers of M1 (Fig. 4H). The CF size profile across cortical depth, with M2 layer V projecting M1 superficial and deep layers (Fig. 4I), further emphasizes this layer-specific communication pattern.

### Higher number of samples in uFLARE improves top-down/bottom-up discrimination

The clarity of the layer-to-layer connectivity profiles improved as the temporal resolution of data acquisition increased (Figs. S8–S11). In an independent study, we scanned three animals during spontaneous activity using three different TRs with adjusted Ernst angles (TR = 850 ms, 165 ms, and 55 ms). All other parameters were kept identical to those in the original uFLARE high spatial resolution acquisition. Figure S9 shows the functional

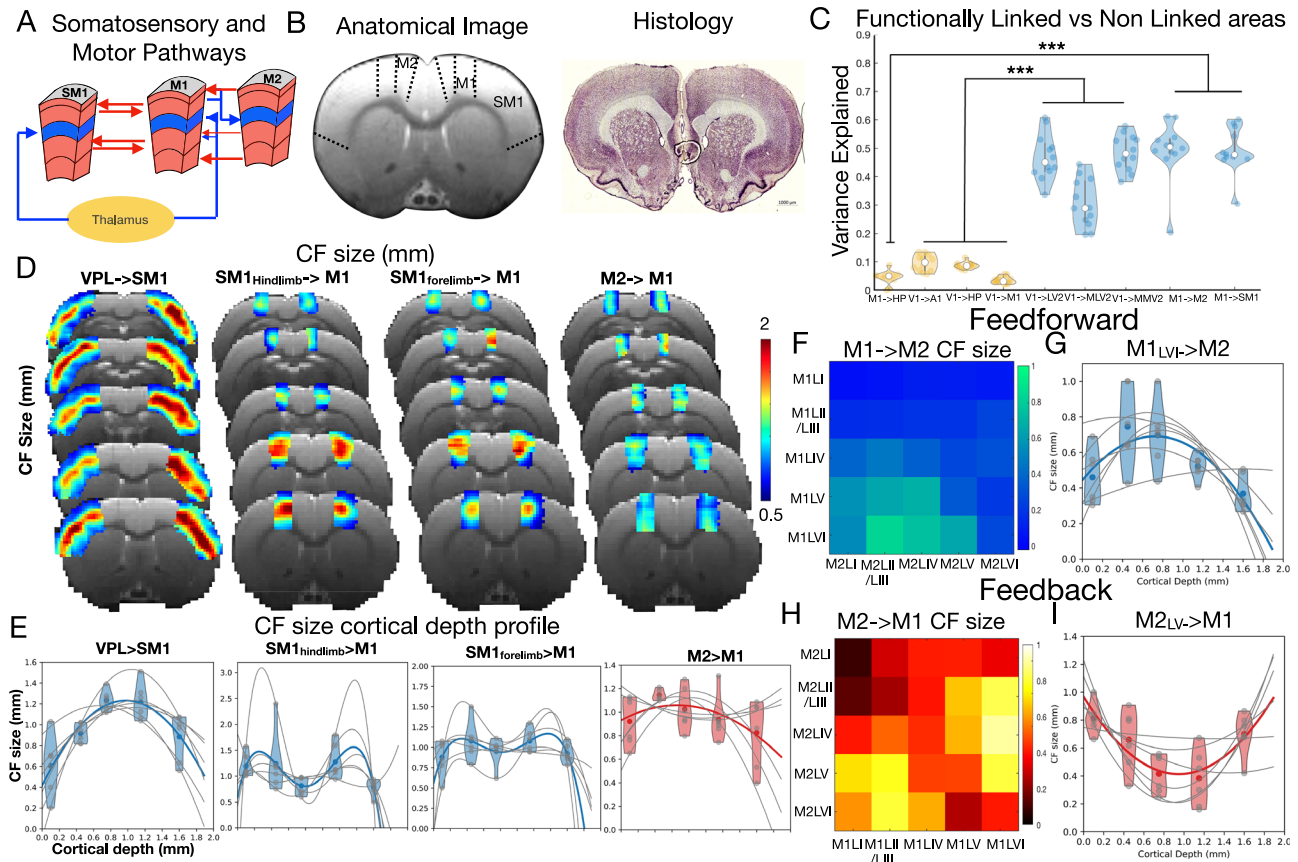


**Fig. 4 | Connectivity in the somatosensory and motor cortices.** **A** Schematic representation of the somatosensory and motor pathways. **B** Anatomical image and histological slice of the somatosensory and motor cortices. **C** Variance explained obtained from brain regions anatomically and/or functionally connected (blue) and brain regions that are not directly connected (yellow) (A1: Primary Auditory Cortex; HP: Hippocampus). The dots (yellow and blue) represent the average variance explained per ROI from each hemisphere of each individual animal ( $n = 6, 12$  hemispheres). The white dot represents the median and the gray line the 1st and 3rd quartiles. The \*\*\* represents a  $p$  value  $< 0.001$ , \*\* $p$  value  $< 0.01$ , and \* $p$  value  $< 0.05$ , resulting from a two-sided  $F$ -test ( $F(1,70) = 326.21, p < 2e-16$ ). **D** Visualizations of CF size averaged across animals projected into the brain slice for the following connections: VPL  $\rightarrow$  SM1; SM1 (forelimb and handlimb)  $\rightarrow$  M1; and M2  $\rightarrow$  M1. **E** CF size

profile (normalized to the mean) across the cortical layers of SM1 and M1 for the following connections: VPL  $\rightarrow$  SM1; SM1 (forelimb and handlimb)  $\rightarrow$  M1; and M2  $\rightarrow$  M1. The gray dots represent the data from each individual animal, and the gray lines represent the parabolic fit per animal. The blue or red dots and lines represent the median of all animals. **F** Bottom-up connections between M1 and M2 layers acquired under spontaneous activity. **G** The CF size profile (normalized to the mean) demonstrates projections from M1 layer VI to all M2 cortical layers. **H** Top-down connections between M2 and M1 layers acquired under spontaneous activity. **I** The CF size profile (normalized to the mean) demonstrates projections from M2 layer V to all M1 cortical layers. Source Data has been included as a Source Data file.

images and representative time series acquired at each TR. Figures S10 and S11 present the bottom-up and top-down connectivity maps for each temporal resolution between V1  $\leftrightarrow$  Lateral V2 area (LV2) (Fig. S10) and V1  $\leftrightarrow$  Medial Lateral V2 area (MLV2) (Fig. S11). At TR = 850 ms, we cannot clearly distinguish bottom-up connections, characterized by larger CF sizes in the middle layers of V2, from top-down inputs from V2, particularly from LI, projecting to the deepest and most superficial layers of V1. At this temporal resolution, the U-shaped and inverted U-shaped CF size profiles exhibited shallow parabolic coefficients and high variability across animals. As temporal resolution increased, the connectivity maps revealed clearer distinctions between bottom-up and top-down pathways. In particular, top-down signals became more evident at TR = 165 ms and were even more pronounced at TR = 55 ms. Furthermore, inter-subject variability decreased as TR shortened. At TR = 55 ms, we obtained the most robust maps, with sharply defined CF size profiles that are hallmark signatures of bottom-up and top-down connections. At this resolution, the parabolic coefficients were also the highest. These results were also corroborated by a downsampling analysis of the original standard spatial resolution single-slice data. For both the VC and

motor cortex slices, we downsampled the temporal resolution from 50 ms to 350 ms. At 350 ms, bottom-up connections are no longer distinguishable from top-down (Fig. S8). The loss of specificity in layer-to-layer connectivity maps with decreased temporal resolution is evident in both visual and somatosensory/motor systems (Fig. S8). This lack of precision may partially explain why the area-to-layer projections from M2 to M1 (obtained from multislice data, where TR = 350 ms), on average, did not exhibit a U-shaped profile (Fig. 4E). Other factors that may contribute to the absence of a clear top-down pattern in Fig. 4E include variability in the dynamic organization of M1–M2 connectivity and the fact that our analysis considered projections from all M2 layers to all layers of M1, aggregating across M2 layers may have obscured layer-specific effects.

Moreover, we performed simulations to examine how the number of time points in the series and the sampling frequency affected CF errors in both center and size. Our results showed that, across all three simulated sampling frequencies (0.5 Hz, 1 Hz and 2 Hz), increasing the number of time points consistently reduced CF estimation errors for both the center (Fig. S13A–C) and size (Fig. S13D–F). The simulations also showed that increasing sampling frequency alone did not reduce

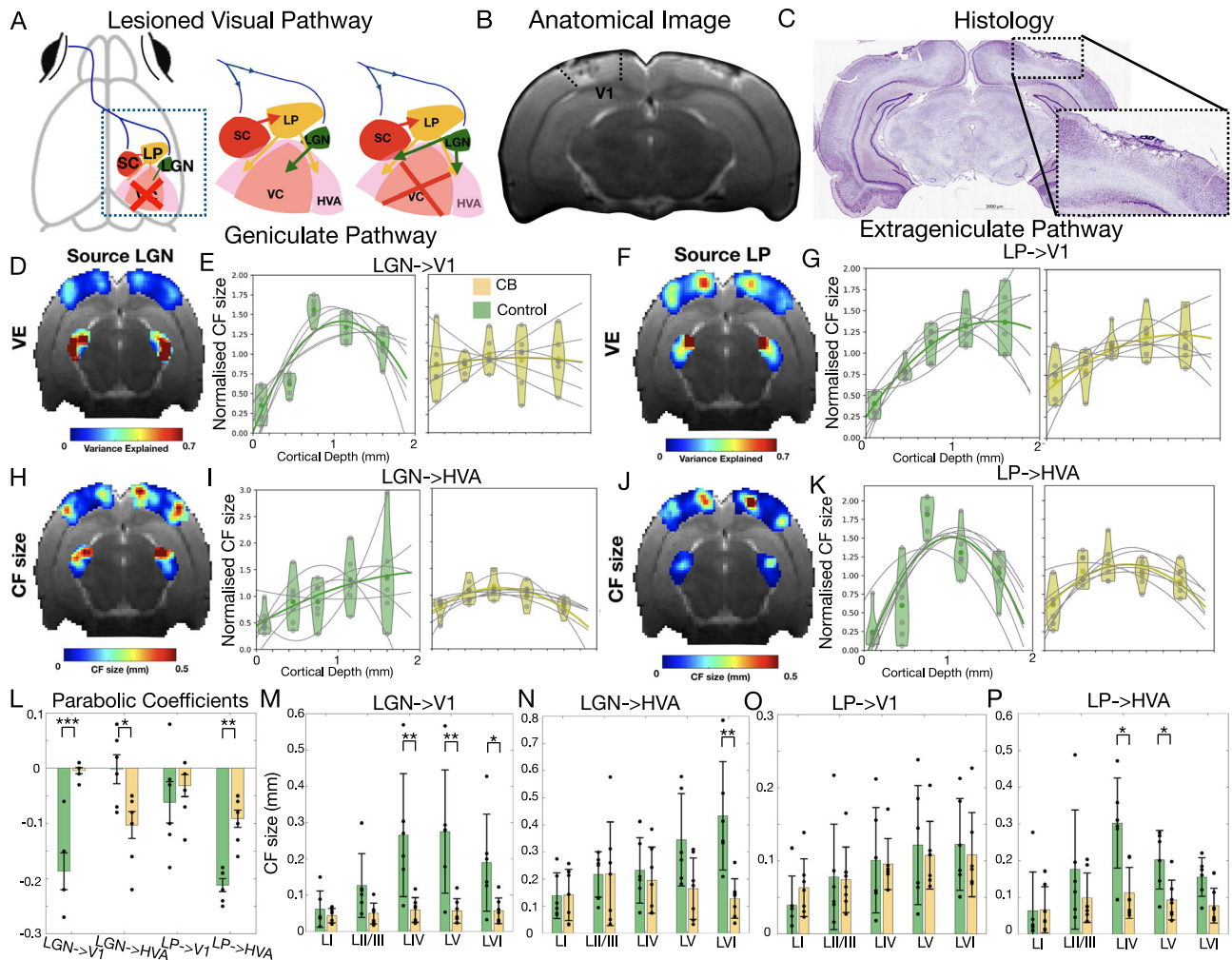


**Fig. 5 | Bottom-up and Top-down profiles following VC Lesions.** **A** Schematic representation of the V1 lesion and expected reorganization of the pathway. The mouse drawing is adapted from Petrucco, L. *Mouse head schema* (2020), Zenodo (<https://doi.org/10.5281/zenodo.3925903>), licensed under CC BY 4.0. **B** Anatomical image illustrating the bilateral V1 lesions. **C** Histological image showing a V1-lesioned animal brain with decreased cell density in the lesion site. **D, F** VE of the CF model averaged across CB animals and computed taking as source LGN and LP, respectively, projected on brain slices. **H, J** CF size averaged across CB animals when LGN and LP are taken as sources, respectively, projected on brain slices. Quantitative analysis of the CF size (normalized to the mean) as a function of cortical depth for HC (green) and for CB animals (yellow) obtained for the connections: LGN → V1 (**E**); LP → V1 (**G**); LGN → HVA (**I**); LP → HVA (**K**). The gray dots represent the data from each individual animal, and the gray lines represent the parabolic fit per animal. The green or yellow dots and lines represent the median of all animals from each group. **L** Quadratic Coefficients obtained for the ICF size profile across cortical layers for controls (green) and CB animals (yellow). The black dots represent the parabolic coefficient from each individual animal. The error bars

represent the mean values ± standard error of the mean (SEM). The \*\*\* represents a  $p$  value < 0.001, \*\*  $p$  value < 0.01, and \*  $p$  value < 0.05 resulting from a two-sided  $F$ -test between the parabolic coefficients of controls and CB animals. LGN → V1 ( $F(1,11) = 28.92, p = 0.0003, d = 5.38$ ); LGN → HVA ( $F(1,11) = 4.87, p = 0.049, d = 1.128$ ) and LP → HVA ( $F(1,11) = 30.3, p = 0.003, d = 3.17$ ). Average CF size per layer calculated for HC (green) and CB (yellow) animals obtained for the connections: LGN → V1 (**M**); LGN → HVA (**N**); LP → V1 (**O**); LP → HVA (**P**). The non-normalized ICF sizes are shown in Fig. S15. The black dots represent the parabolic coefficient from each individual animal. The error bars represent the standard error of the mean. A one way ANOVA corrected for multiple comparisons was performed to investigate the differences in CF size across layers between controls CB animals: LGN → V1 LIV ( $F(1,11) = 8.63, p = 0.01, d = 2.94$ ), LV ( $F(1,11) = 9.84, p = 0.01, d = 3.14$ ) and LVI ( $F(1,11) = 5.81, p = 0.04, d = 2.41$ ); LGN → HVA layer VI:  $F(1,11) = 11.65, p = 0.007, d = 1.97$ ; and LP → HVA Layer IV ( $F(1,11) = 8.55, p = 0.015, d = 1.69$ ); Layer V ( $F(1,11) = 7.33, p = 0.022, d = 1.56$ ). Source Data file.

estimation error. These findings underscore the critical importance of high temporal resolution for accurately capturing the nuanced dynamics of cortical connectivity.

Furthermore, to validate the biological relevance of the CFs, we computed them between brain regions with known anatomical connections, specifically, between visual areas and between motor and somatosensory areas, as well as between regions where strong connections are not expected, such as between the VC and auditory/motor cortex, or the VC and hippocampus. Brain regions with known anatomical connections have much higher VE than regions that are not anatomically or functionally connected

(Fig. 4C). This difference in VE is highly significant ( $F(1,70) = 326.21, p < 2e-16, d = 4.26$ ).

**UFLARE reveals circuit reorganization following cortical lesions**

The ability of ICF estimates to distinguish between bottom-up and top-down pathways opens the possibility of mapping plasticity upon network perturbations, reinforcing their causal validity rather than merely reflecting correlational effects. To test this, we induced cortical blindness (CB) by bilaterally lesioning the V1 region in seven animals (Fig. 5A). Figure 5B, C displays anatomical and histological images of the lesions, with V1 appearing lighter and whitish in color, indicative of

cell death. The layered structure of the cortex is also less distinct. These lesions disrupt the visual pathway, and we expected these changes to be reflected in the CF size profiles. Specifically, we hypothesized that, in the absence of an intact visual pathway, the LGN—which normally projects directly to V1—would instead project to HVA. Additionally, we anticipated that the extrageniculate pathway (LP → HVA) would strengthen its projections, compensating for the loss of the geniculate pathway.

We calculated the area-to-layer CFs seeding from the LP and LGN to predict the VC (V1 and HVA) time series (Fig. 5D–P). The VE of the ICF projecting from LGN and LP to V1 in CB animals was close to zero (VE: LGN → V1 =  $0.04 \pm 0.02$ ; LP → V1 =  $0.03 \pm 0.02$ , Table S3) and highly reduced compared to healthy control (HC) animals (VE: LGN → V1 =  $0.42 \pm 0.05$ ; LP → V1 =  $0.22 \pm 0.07$ ), confirming that CFs capture biologically relevant information (Fig. 5D, F, H, J). We then analyzed CF size profiles across cortical depth. Meaningful bottom-up projections like LP to V2 (in both HC and CB) and LGN to V1 (in HC) displayed an inverted-U-shaped profile. Notably, for the LGN to V1 connection in CB animals, this profile was absent due to the lack of neural activity in V1 (Fig. 5E). Therefore, the parabolic coefficients from the fits of the CF size across cortical layers are highly significantly different between HC and CB animals ( $F(1,11) = 28.92$ ,  $p = 0.0003$ ,  $d = 5.38$ ) (Fig. 5L). In addition, there are significant changes in CF size in V1 LIV ( $F(1,11) = 8.63$ ,  $p = 0.01$ ,  $d = 2.94$ ), LV ( $F(1,11) = 9.84$ ,  $p = 0.01$ ,  $d = 3.14$ ) and LVI ( $F(1,11) = 5.81$ ,  $p = 0.04$ ,  $d = 2.41$ ) between HC and CB animals when the source is LGN (Fig. 5M).

Interestingly, the LGN to HVA connection in CB animals showed an emerging inverted U-shaped pattern (Fig. 5I), which was not present in HC (linear trend), suggesting potential compensatory changes in the visual pathway following the V1 lesion. This resulted in significant changes in the parabolic coefficient from the fits of the CF size across cortical layers between HC and CB animals ( $F(1,11) = 4.87$ ,  $p = 0.05$ ,  $d = 1.28$ ) (Fig. 5L), with CB animals showing a more negative parabolic coefficient. Furthermore, there were significant changes in CF size in HVA layer VI between HC and CB animals when the source is LGN ( $F(1,11) = 11.65$ ,  $p = 0.007$ ,  $d = 1.97$ ) (Fig. 5N).

In contrast, non-meaningful connections, such as LP to V1, exhibited a linear increase in CF size with cortical depth for both HC and CB groups, with no significant differences in the parabolic coefficients ( $F(1,11) = 0.04$ ,  $p$  value = 0.85,  $d = 0.12$ ), neither on the average CF size obtained per layers ( $p$  value > 0.05) between HC and CB animals (Fig. 5G, L, O).

The projection from LP to V2 shows an inverted-U-shaped profile for both HC and CB (Fig. 5K); however, the curvature of the parabolic fit obtained for the CB is shallower than the one obtained for the HC ( $F(1,11) = 30.3$ ,  $p = 0.003$ ,  $d = 3.17$ ) (Fig. 5L). The CF size in layer IV and V is significantly higher in HC than in CB animals ( $F(1,11) = 8.55$ ,  $p = 0.015$ ,  $d = 1.69$ ;  $F(1,11) = 7.33$ ,  $p = 0.022$ ,  $d = 1.56$  respectively) (Fig. 5P).

Two additional animals were monocularly lesioned. Figure S16 shows that in the spared hemisphere, the ICF size calculated from LGN to V1 shows larger CF sizes in Layer IV. In the lesioned site, CF size and VE are significantly decreased (VE = 0) and the CF size increases in the HVAs surrounding the lesion.

## Discussion

We introduced uFLARE fMRI and showed that its connectivity signatures are associated with bottom-up and top-down processes across cortical layers. The dissociation of bottom-up and top-down signals from spontaneous activity non-invasively with fMRI opens new ways of characterizing information flow in the brain. As predicted in ref. 58, we found that CF size—a measure of information integration—produces two distinct connectivity profiles across cortical layers. Bottom-up connectivity was characterized by an inverted U-shaped pattern, with larger CF sizes concentrated in LIV; while top-down connectivity exhibited a U-shaped profile, with CF sizes peaking in the superficial

(LI) and deep (LVI) cortical layers. The ICF size profiles are in line with our understanding of underlying neural functional and anatomical architecture, i.e., axonal projections<sup>41,70</sup>. Importantly, we have shown that ICF profiles associated with bottom-up and top-down are general, as observed in different brain sensory systems (somatosensory, motor and visual), and that they provide meaningful insight into information flow upon injury (as observed in the CB animal model), suggesting it may have high relevance for understanding disease progression, recovery from injury, development, and plasticity, among other applications.

Bottom-up signals are generally considered to carry sensory information, while top-down signals reflect top-down expectations or predictions<sup>71,72</sup>. However, uFLARE's ability to dissociate bottom-up and top-down signals during spontaneous activity challenges the notion that bottom-up signals are exclusively stimulus-dependent. Instead, the dissociation of bottom-up and top-down signals during spontaneous activity suggests that laminar-specific bottom-up and top-down interactions are continuously active and interacting. This is consistent with studies showing that cortical responses to natural stimulation closely resemble those observed during spontaneous activity<sup>66</sup> and that the network structure distinguishing bottom-up and top-down-specific neurons persists even without stimulation<sup>73</sup>. These findings support the view that spontaneous activity reflects the underlying connectivity and the balance between bottom-up and top-down signals.

The area-to-layer CF patterns primarily reflect the bottom-up pathway, highlighting the complementary roles of the geniculate (retina → LGN → V1) and extrageniculate (retina → SC → LP → HVA) pathways in visual processing<sup>74</sup>. The LGN and LP provide targeted input to the middle layers of V1 and HVA, respectively. When we repeated the area-to-layer analysis using FC, for the LGN → V1 connection, the inverted U-shaped profile was still evident, suggesting that increasing either sample size or scan duration may achieve sufficient specificity for reliably detecting area-to-layer profiles with FC. Additionally, CF maps derived from spontaneous activity in both geniculate and extrageniculate pathways demonstrated a clear visuotopic organization. This underscores that CF is a stimulus-agnostic tool, enabling the study of sensory topography and the underlying bottom-up and top-down mechanisms in the absence of external stimulation<sup>58,75</sup>. This finding is consistent with CF studies in humans, where similar retinotopic maps were estimated from both task-based data (e.g., movie watching) and spontaneous activity data<sup>61,62</sup>.

Furthermore, for animals with bilateral cortical lesions in V1 (Cortical Blindness group), the ICF estimates revealed that bottom-up input from the LGN bypasses V1 and is directed to HVAs, following an inverted U-shaped CF size profile. This finding aligns with invasive V1 lesion studies in both rodents and humans. In rodents, it has been shown that after a V1-induced lesion, LGN neurons project directly to several HVAs<sup>74,76</sup>. Future studies should cross-validate these plasticity changes with ground-truth measurements, such as retrograde viral tracing to identify the sensory FF and FB pathways in lesioned animals. Nevertheless, previous studies using neural tract tracing to investigate how neural circuits reorganize following V1 lesions point in the same direction as our findings. In non-human primates, both the pulvinar<sup>77</sup> and the LGN<sup>78</sup> have been shown to play key roles in bypassing V1 damage and providing direct input to higher-order areas such as the middle temporal (MT) visual area. Moreover, in humans, residual vision—such as blindsight—following V1 injury is thought to be mediated by circuits that bypass V1, directly relaying signals to higher-order cortical areas<sup>79</sup>. These results suggest that the distinct properties of these visual areas depend on inputs from regions beyond V1, indicating the existence of an adaptive alternative pathway that maintains visual processing despite the loss of primary visual input.

Importantly, all animals were adults (8–24 weeks old) at the time the lesions were performed and when the MRI scans were acquired.

This supports the view that the rat visual pathway retains plasticity beyond the classical critical period. These findings align with previous studies demonstrating substantial post-critical period plasticity in rodents, both within the visual system<sup>80,81</sup> and in the somatosensory cortex<sup>80</sup>. Notably, Yu et al. reported that plasticity beyond the critical period appears to be primarily mediated by subcortical-to-cortical pathways, such as thalamocortical projections, rather than by cortico-cortical connections<sup>80</sup>. Consistent with this, our results suggest that the observed plasticity is likewise driven by subcortical-to-cortical connections, specifically from the LGN to VC.

Our work highlights the essential role of fast imaging and applying bidirectional computational models of information flow within cortical networks for disentangling bottom-up and top-down patterns. Importantly, to achieve layer specificity and resolve the “directionality” of signals, we need both uFLARE’s high spatial resolution and ultrafast nature. In our view, there are three main reasons why rapid imaging leads to layer specificity and allows us to infer directionality of information flow. First, ultrafast acquisition yields a greater number of data points, enabling a better sampling of the underlying neural activity—in particular infra-slow spontaneous neuronal activity—and consequently, a more robust model fitting. Such activity has been shown to be unevenly distributed across cortical layers in the resting brain<sup>82</sup>. Mitra and colleagues further demonstrated that infra-slow spatio-temporal trajectories in blood oxygen signals closely align with infra-slow dynamics measured using calcium imaging and electrophysiology<sup>83</sup>. This provides strong evidence that spontaneous BOLD signals reflect a genuine infra-slow neural process, rather than merely arising from vascular low-pass filtering of higher-frequency activity. Furthermore, more data points significantly improve the accuracy of the model fitting. Our simulations showed that, independently of the sampling frequency used, increasing the number of time points consistently reduced the error associated with the CF estimates. Our simulations are in line with recent studies that have shown that longer scans (with more time points) enhance predictive power<sup>84</sup>, and that increasing fMRI temporal resolution improves the performance of directional sensitive models, i.e., Granger Causality<sup>85</sup>. uFLARE inherently leads to ultrafast sampling of hemodynamic response, which in itself has been shown to encode specific neural information. In particular, Chuang et al. recently demonstrated in a combined ultrafast fMRI and electrophysiology study that hemodynamic timing and shape reflect excitatory/inhibitory neuronal density and cortical hierarchy, thereby providing valuable information about information flow<sup>86</sup> in cortical circuits<sup>50,87</sup>. This suggests a paradigm shift in the current fMRI studies attempting to dissociate bottom-up and top-down signals, which currently focus on layer selectivity (high spatial resolution), overlooking the temporal resolution. However, we acknowledge that sacrifices of spatial coverage may be necessary to achieve this temporal resolution, although parallel mapping methods<sup>88–92</sup> are likely to become highly useful for achieving both spatial and temporal high resolution, simultaneously. Furthermore, although spontaneous BOLD oscillations have traditionally been considered functionally relevant within the lower frequency range (0.01–0.1 Hz<sup>93</sup>), we show that resting-state dynamics may extend across a broader frequency spectrum than previously assumed. In particular, relevant information about bottom-up and top-down signals appears to be encoded at frequencies above those typically analyzed in resting-state studies. This observation is consistent with recent reports showing that frequencies above 0.1 Hz also contribute to resting-state networks<sup>92</sup> and that strong oscillations can be detected up to 0.3 Hz<sup>50,87</sup>. Future investigations of spontaneous activity should therefore consider a broader frequency range and/or employ denoising techniques that eliminate the need for strict frequency filtering.

As in every study, our work has several limitations. First, isolating top-down signals, i.e., using attentional or imagery tasks, is challenging in rodents and preclinical scanners. While bottom-up and top-down

signals coexist during both stimulation and spontaneous activity, a top-down-specific task could help confirm the U-shaped top-down profile. However, previous research suggests spontaneous activity is predominantly top-down-driven<sup>66</sup>. Second, the sedation regime used in our work likely weakens neural activity in higher-order areas, potentially suppressing top-down signals and biasing ICF estimates. Although the animals were sedated throughout, a study by Semedo et al. found that top-down responses persist under anesthesia, suggesting top-down activity is not entirely abolished<sup>22</sup>. Furthermore, our sedation regime closely resembles the awake state in terms of neurovascular coupling<sup>50,94</sup> and basic function<sup>95</sup>. Looking ahead, repeating this experiment in awake animals, where the effects observed here would likely be comparable, if not stronger, will be important. Third, the lesions in this study, while spatially localized, may have effects beyond the target area. Future studies could refine the analysis of top-down signals by optogenetically stimulating V2, isolating top-down mechanisms without influencing bottom-up activity. Fourth, potential bias in the CF estimation due to the size of the source ROI: when the CF center approaches the border of the source ROI, edge effects can occur, leading to an artificial reduction in CF size<sup>58</sup>. Fifth, hemodynamic response function (HRF) effects: in fact, the CF model does not directly rely on assumptions about the HRF, because it correlates features at the signal level. However, hemodynamic signals vary across cortical depth, with the fastest hemodynamic responses occurring in the deep layers, whereas the slowest responses are observed in layer I<sup>96</sup>. These differences in HRF timing across layers—linked to spatial gradients in microvascular dilation delays—could, in principle, influence layer-dependent CF estimates, as signals with similar HRF characteristics are therefore expected to show higher correlations. However, the variation in HRF with cortical depth is relatively small, with peak times ranging only from 3.2 to 2.5 s<sup>96</sup>. In practice, the effect on ICF is small, particularly in the absence of stimulus-driven activity. Indeed, when we simulated spontaneous fMRI activity using HRFs from LI and LIV—that exhibit the most distinct dynamics across cortical layers<sup>96</sup> (c.f. Fig. S14 for HRF profiles)—the observed differences in CF properties were minimal: the average variation in CF size is 0.024 mm and the error in CF center is approximately 2 voxels, indicating that the variation of HRF with cortical depth, even when the underlying HRF’s are maximally different, has a negligible effect on CF estimates (Fig. S14B, C). Furthermore, if HRF differences were dominant in our ICF results, one would expect CF to primarily link layers with similar HRF properties, for instance, V1 LI with V2 LI, and V1 LVI with V2 LVI, independent of whether the signals are bottom-up or top-down. Importantly, we do not observe such a pattern. Moreover, variations in HRF across cortical depth cannot account for the characteristic parabolic profiles (U-shaped and inverted U-shaped) of top-down and bottom-up signals, which cannot be explained solely by vascular differences across layers. Sixth, to achieve fast imaging on the order of 50 ms while maintaining sufficient SNR, we are constrained to acquiring a single slice. If it were possible to include more slices within the same TR without compromising SNR, this would significantly enhance coverage and represent a clear advantage. At present, hardware limitations prevent this; however, simultaneous multi-slice (SMS) approaches<sup>97</sup> may alleviate some of these constraints in future studies. Seventh, single-slice acquisitions may be more susceptible to inflow-related vascular signals, whereas multislice acquisitions can, in contrast, introduce saturation effects from neighboring regions. In our experience, even when using slightly shorter TRs, the observed effects persist with multislice acquisitions. This suggests that they are unlikely to be solely attributable to inflow or outflow effects. Eighth, in the future, we should investigate the SNR/tSNR threshold that allows the uFLARE to capture the directionality of information flow from RS data. Nonetheless, in the present work, we are confident that the SNR is sufficient to obtain reliable CF estimates. First, the topography analysis clearly reveals the retinotopic organization of the visual system.

Second, the model explains a substantial proportion of variance overall, and poorly fitting voxels are excluded through thresholding. Ninth, here we used ultrafast BOLD signals, while non-BOLD fMRI techniques such as VASO and MION-CBV offer greater layer specificity they require longer acquisitions, which are critical for separating bottom-up from top-down signals. Tenth, we applied the ICF method between predefined visual areas, but it can, in principle, be extended across the entire brain without predefined ROIs. However, this approach results in a large search space. To address this limitation, we are currently developing more efficient GPU-based implementations.

Noninvasively disentangling bottom-up and top-down signals in rodents enables pathway-wide investigations without requiring viral injections or electrode placements, which may alter neural activity. Furthermore, with advancements in high-resolution MRI, this approach could be extended to high-field clinical scanners. The ability of uFLARE to non-invasively dissociate bottom-up and top-down connections from spontaneous activity offers exciting opportunities to explore the bottom-up/top-down balance in humans. Understanding the bottom-up/top-down dynamics is crucial, as disruptions contribute to conditions such as schizophrenia, hallucinations, autism spectrum disorder (ASD), depression, attention-deficit/hyperactivity disorder (ADHD), and post-traumatic stress disorder (PTSD). Tracking bottom-up and top-down signals could also enhance our understanding of action planning, attention, predictive coding, and contextual modulation. Clinically, detecting bottom-up/top-down imbalances may improve diagnostics and inform targeted interventions, such as neuromodulation or cognitive therapies, to restore proper communication.

## Methods

All the experiments strictly adhered to the ethical and experimental procedures in agreement with Directive 2010/63 of the European Parliament and of the Council, and were preapproved by the competent institutional (Champalimad Animal Welfare Body) and national (Direção Geral de Alimentação e Veterinária, DGAV) authorities.

In this study, we conducted two distinct sets of experiments to investigate bottom-up and top-down circuits: (1) in the VC of healthy and cortically lesioned animals; and (2) in the somatosensory and motor cortices of healthy animals.

Regarding the experiments probing the visual pathway, a total of 19 Long Evans rats (12 controls: 10 F, 12–30 weeks old,  $w = 412 \pm 75$  g; and 7 rats for the lesion experiment: 5 F, 8–24 weeks old,  $w = 364 \pm 45$  g) were scanned in two separate sessions. Session 1 focused on retinotopic mapping, while Session 2 involved ultrafast acquisitions. In Session 2, three sets of ultrafast experiments were conducted to investigate bottom-up and top-down connectivity in the visual system of rats: set 1—Standard spatial resolution RS scans in control animals ( $N = 6$ ); set 2—High spatial resolution scans (both RS and visual stimulation) in control animals ( $N = 6$ ); set 3—Standard spatial resolution RS scans in the rats with lesions in the VI. Except for the cortical lesions experiment (set 3), Session 1 took place 1 week before Session 2.

In the experiments probing the somatosensory and motor cortices, six Long Evans Rats (4 F, 11–15 weeks old,  $w = 423 \pm 69$  g) were scanned.

## Animal preparation

All in vivo experiments were performed under sedation. The animals were induced into deep anesthesia in a custom box with a flow of 5% isoflurane (Vetflurane, Virbac, France) mixed with oxygen-enriched (27%) medical air for ~2 min. Once sedated, the animals were moved to a custom MRI animal bed (Bruker Biospin, Karlsruhe, Germany) and maintained under ~2.5–3.5% isoflurane while being prepared for imaging. Eye drops (Bepanthen, Bayer, Leverkusen, Germany) were applied to prevent the eyes from drying during anesthesia.

Approximately 5 min after the isoflurane induction, a bolus (0.05 mg/kg) of medetomidine (Dormilan, Vetpharma Animal Health, Spain), consisting of a 1 mg/ml solution diluted 1:10 in saline, was administered subcutaneously. Ten to eighteen minutes after the bolus, a constant infusion of 0.1 mg/kg/h of medetomidine, delivered via a syringe pump (GenieTouch, Kent Scientific, Torrington, Connecticut, USA), was started. During the period between the bolus and the beginning of the constant infusion, isoflurane was progressively reduced until 0%.

Temperature and respiration rate were continuously monitored via a rectal optic fiber, temperature probe, and a respiration sensor (Model 1025, SAM-PC monitor, SA Instruments Inc., USA, respectively), and remained constant throughout the experiment. Each MRI session lasted between 2 h 30 min and 3 h. At the end of each MRI session, to revert the sedation, 2.0 mg/kg of atipamezole (5 mg/ml solution diluted 1:10 in saline) (Antisedan, Vetpharma Animal Health, Spain) was injected subcutaneously at the same volume as the initial bolus.

## MRI acquisition

All the MRI scans were performed using a 9.4 T Bruker BioSpin MRI scanner (Bruker, Karlsruhe, Germany) operating at a  $^1\text{H}$  frequency of 400.13 MHz and equipped with an AVANCE III HD console and a gradient system capable of producing up to 660 mT/m isotropically. An 86 mm volume quadrature resonator was used for transmittance. A 20 mm loop surface coil and a 4-element array cryoprobe (Bruker, Fallanden, Switzerland) were used for signal reception during Session 1 and Session 2 of visual system experiments, respectively. The cryogenic reception coil was also used for the somatosensory and motor cortex experiments. The software running on this scanner was ParaVision<sup>®</sup> 6.0.1.

After placing the animal in the scanner bed, localizer scans were performed to ensure that the animal was correctly positioned, and routine adjustments were performed.  $B_0$  maps were acquired. A high-definition anatomical  $T_2$ -weighted Rapid Acquisition with Refocused Echoes (RARE) sequence (TE/TR = 13.3/2000 ms, RARE factor = 5, FOV =  $20 \times 16$  mm<sup>2</sup>, in-plane resolution =  $80 \times 80$   $\mu\text{m}^2$ , slice thickness = 500  $\mu\text{m}$ ,  $t_{\text{acq}} = 1$  min 18 s) was acquired for accurate referencing. Importantly, the functional MRI scans were started ~30 min after the isoflurane was removed from the breathing air to avoid the potentially confounding effects of isoflurane<sup>98</sup>.

## Visual system experiments

### Session 1: retinotopy

**Acquisition.** Functional scans were acquired using a gradient-echo echo-planar imaging (GE-EPI) sequence (TE/TR = 12/1500 ms, FOV =  $20.5 \times 20.5$  mm<sup>2</sup>, resolution =  $227 \times 227$   $\mu\text{m}^2$ , slice thickness = 788  $\mu\text{m}$ , 8 slices covering the visual pathway, flip angle = 15°). The animals underwent a total of 6 runs of the retinotopic stimulus, each run taking 7 min and 39 s to acquire (306 repetitions). In addition, a 10 min RS scan was also acquired with the same parameters.

**Stimulus and setup.** The visual stimuli consisted of a luminance contrast-inverting checkerboard drifting bar<sup>48</sup>. The bar aperture was composed of alternating rows of high-contrast luminance checks moved in 8 different directions (4 bar orientations: horizontal, vertical, and the two diagonal orientations, with two opposite drift directions for each orientation). The bar moved across the screen in 16 equally spaced steps, each lasting 1 TR. The bar contrast, width, and spatial frequency were 50%, -14.5°, and -0.2 cycles per degree of visual angle (cpd), respectively. The retinotopic stimulus consisted of four stimulation blocks. At each stimulation block, the bar moved across the entire screen during 24 s (swiping the visual field in the horizontal or vertical directions) and across half of the screen for 12 s (swiping half of the visual field diagonally), followed by a blank full-screen stimulus at mean luminance for 45 s. A single retinotopic mapping run consisted

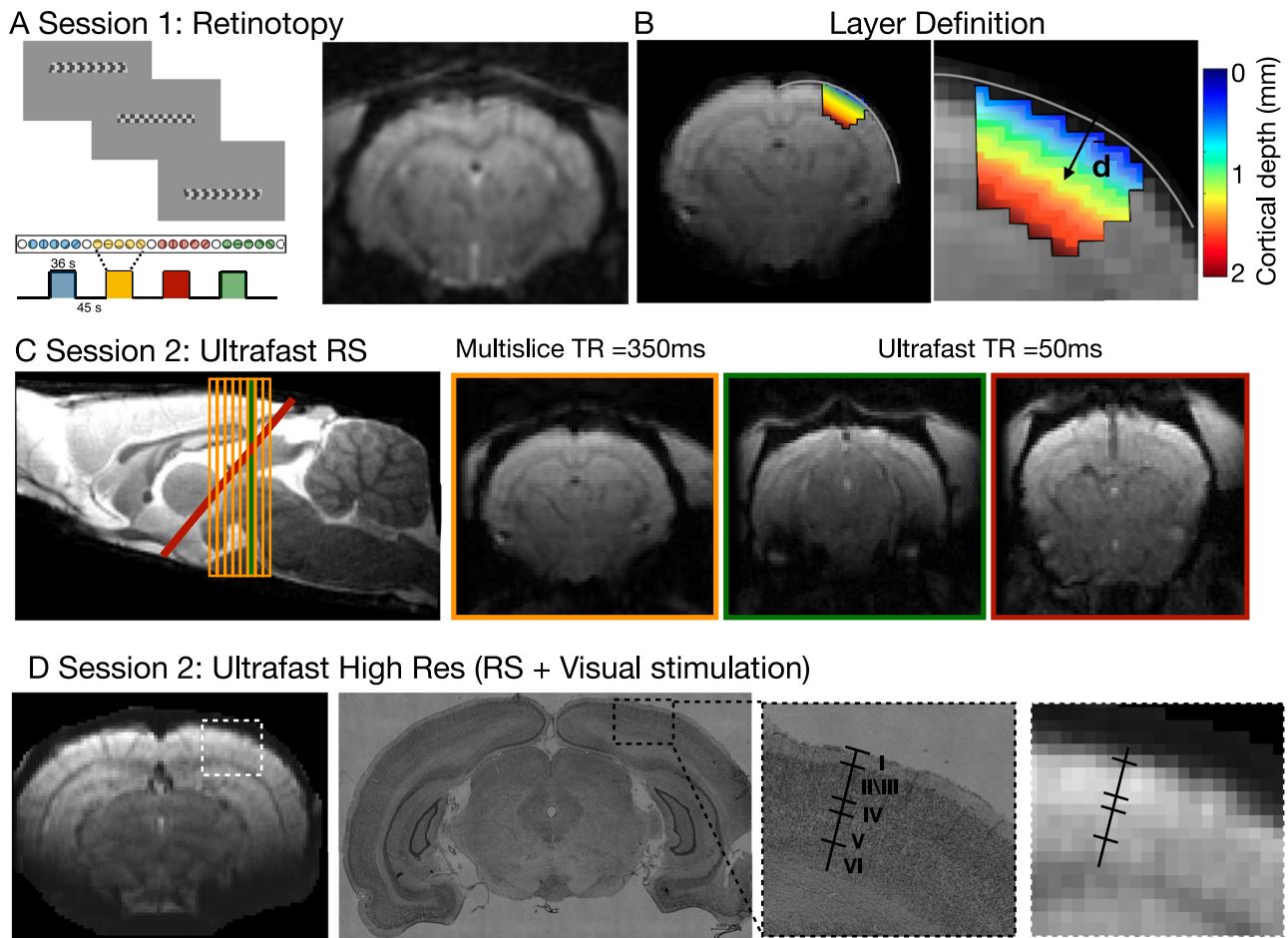


**Fig. 6 | MRI acquisition protocol. A** Retinotopic stimulus, stimulation paradigm and an example of a slice acquired in Session 1. **B** Representative functional slice acquired in Session 2 (Standard Resolution) and its respective layer definition (where  $d$  is the distance from cortical surface). **C** Representative functional slices of

the RS datasets (multislice (orange), single VC slice (green) and single VP slice (red)) acquired at standard resolution. **D** High spatial resolution VC slice acquisition and histology analysis of a HC animal with the layer definition.

of 246 functional images (60 pre-scan images were deliberately planned to be discarded due to coil heating).

The complex visual stimuli necessary for retinotopic mapping were generated outside the scanner and back-projected with an Epson EH-TW7000 projector onto a semitransparent screen positioned 2.5 cm from the animals eyes. The setup has been previously described<sup>48</sup>. Visual stimuli were created using MATLAB (Mathworks, Natick, MA, USA) and the Psychtoolbox. An Arduino MEGA260 receiving triggers from the MRI scanner was used to control stimuli timings.

**Session 2: standard spatial resolution RS in control animals.** Three ultrafast RS datasets were obtained using GE-EPI acquisitions from: a multislice set; a VC slice and a visual pathway (VP) slice (Fig. 6C).

**Multislice set.** The functional MR imaging was acquired using a GE-EPI sequence (TE/TR = 12/350 ms, FOV =  $20.5 \times 20.5$  mm<sup>2</sup>, resolution =  $227 \times 227$   $\mu$ m<sup>2</sup>, slice thickness = 788  $\mu$ m, 8 slices,  $t_{acq}$  = 20 min 500 ms).

**VC and VP slices.** The functional MR imaging was acquired using a GE-EPI sequence (TE/TR = 11.6/50 ms, FOV =  $20.5 \times 20.5$  mm<sup>2</sup>, resolution =  $227 \times 227$   $\mu$ m<sup>2</sup>, slice thickness = 788  $\mu$ m,  $t_{acq}$  = 20 min 500 ms).

**Session 2: ultra-high spatial resolution spontaneous activity and visual stimulation in control animals.** Two high spatial resolution

ultrafast datasets of the VC were obtained: one during RS and one during visual stimulation. The functional MR imaging was acquired from the VC slice defined above using a GE-EPI sequence (TE/TR = 14.7/55 ms, FOV =  $18 \times 16$  mm<sup>2</sup>, resolution =  $164 \times 165$   $\mu$ m<sup>2</sup>, slice thickness = 700  $\mu$ m,  $t_{acq}$  = 20 min 500 ms). To avoid contamination of the visual stimulation effect to the RS, the RS scan was acquired before the visual stimulation scan.

**Visual stimulation.** A bifurcated optic fiber connected to a blue LED ( $\lambda$  = 470 nm and  $I$  =  $8.1 \times 10^{-1}$  W/m<sup>2</sup>) was placed horizontally in front of each eye of the animal (spaced up to 1 cm) for binocular visual stimulation. The blue LED was connected to an Arduino MEGA260, receiving triggers from the MRI scanner, and was used to generate square pulses of light. A stimulation frequency of 8 Hz was used. The LEDs flickered continuously during the entire duration of the scan.

**Session 2: standard spatial resolution RS in lesioned animals.** The MRI acquisition of lesioned animals was identical to that obtained for controls (see Section “Session 2: standard spatial resolution RS in control animals”). Session 1 took place 1 week prior to the lesion surgery and the animals were scanned 1 week post-lesion for Session 2.

**V1 lesions: ibotenic acid.** To investigate how bottom-up and top-down pathways were reorganized following V1 lesions,  $n$  = 7 animals were injected bilaterally with an ibotenic acid (Abcam, Romania)

solution (excitotoxic agent, 1 mg/100  $\mu$ L) in the V1. The acid was injected using a Nanojet II (Drummond Scientific Company). Animals were anesthetized with isoflurane (anesthesia induced at 5% concentration and maintenance below 3%), and a scalpel incision was made along the midline of the skull, the skin retracted, and the soft tissue cleaned from the skull with a blunt tool.

Coordinates for the craniotomies and amounts required for the injections were determined for each individual animal based on T2-weighted anatomical images acquired before the surgery. We injected in five different AP (anterior-posterior) coordinates; two injection pulses on the one injection site for the first AP coordinate; and 4 injection pulses for each of the following injection sites, two per AP coordinate, for full coverage of V1. Each injection pulse was administered at a rate of 23 nL/s with 2–3 s between pulses, and each pulse consisted of 32 nL. Waiting time before removing the injection pipette after the last pulse was 10 min. The craniotomies were then covered with Kwik-Cast™ (World Precision Instruments, USA) and the scalp was sutured. Before the animals recovered from surgery, they were injected subcutaneously with 5 mg/kg body weight of carprofen (Rimadyl®, Zoetis, U.S.A). Following surgery, the animals were allowed to recover for around 7 days to avoid MRI acquisition artefacts due to potential inflammation and mechanical damage from the pipette.

**Histology.** Histological analysis was performed for one control and two V1 lesioned animals. Animals were perfused transcardially, -24 h after Session 2. First with a PBS 1X solution, followed by 4% PFA. The brain was extracted and kept in 4% PFA for approximately 12 h. After this, the brain was placed in a 30% sucrose solution for a minimum of 4 days, after which the tissue was embedded in a frozen section compound (FSC 22, Leica Biosystems, Nussloch, Germany) and sliced on a cryostat (Leica CM3050S, Leica Biosystems, Nussloch, Germany). After sectioning, the brain slices were stained with cresyl violet, mounted with Mowiol mounting medium, and imaged using a Zeiss AxioImager M2.

### Somatosensory and motor system experiments

Regarding the experiments probing the somatosensory and motor pathways, a multislice set and a single slice covering the somatosensory and motor pathways were acquired during RS. The scanning parameters are the same as in the multislice and single slice ultrafast acquisitions described in Section “Session 2: standard spatial resolution RS in control animals”.

### Data analysis

#### Preprocessing

**Retinotopy data.** Images were extracted from the scanner using the vendor image reconstruction pipeline and converted to Nifti. Outlier correction was performed (time points whose signal intensity was 3 times higher or lower than the standard deviation of the entire time course were replaced by the mean of the 3 antecedent and 3 subsequent time points).

**Ultrafast data.** The complex data from each cryoprobe channel was extracted and transformed into k-space, where zero filling was removed. Afterward, the images were reconstructed back into image space, and outlier correction was carried out by manually identifying time points with average brain signals deviating  $\pm 2$ –3 standard deviations from a 2nd-order polynomial trend. Subsequently, new voxel values for these outlier time points were estimated using piecewise cubic interpolation based on the remaining time points. This correction was performed slice by slice. Next, we performed thermal noise removal using NORDIC denoising with a sliding window of [5, 5, 1], treating each channel separately. After denoising, zero filling was reintroduced, and the data from the four channels were combined to form the final magnitude images. This procedure enhances sensitivity

for detecting the small BOLD signal fluctuations and weak temporal correlations associated with low tSNR and subtle neuronal activations<sup>99</sup>. Previous studies have demonstrated that denoising yields substantial benefits, including SNR and tSNR gains up to 27% and 100%, respectively, and increases in Fourier spectral amplitude of BOLD maps<sup>99,100</sup>. Importantly, denoising has been shown to be a critical step in the detection of laminar-specific neural networks, in particular using ultra-high field preclinical scanners. Nonetheless, one must remain cautious about the potential risk of over-denoising-driven artifactual activation spreading<sup>100</sup>.

#### Preprocessing steps common to the retinotopy and ultrafast data.

All the following preprocessing steps were performed using a home-written Python pipeline using Nipype.

Simultaneous motion and slice timing correction were performed using Nipy's SpaceTimeRealign function<sup>101</sup>. Brain extraction was done using AFNI function Automask applied to a bias field corrected (with ANTs) mean functional image. The skull stripped images were inspected, and upon visual inspection, a further mask was manually drawn when needed using a home-written script. The skull stripped images then underwent co-registration and normalization to an atlas<sup>102</sup>. Manual co-registration was performed using ITK SNAP, aligning the mean functional image of each run to the anatomical image. Normalization was performed by calculating the affine transform matrix that aligns each anatomical image with the atlas template using ANTs. The two sets of transform matrices were then refined and applied to all the functional images using ANTs.

Following normalization, for Session 1 data (retinotopy), the voxels' signals were detrended using a polynomial function of factor 2 fitted to the resting periods and spatially smoothed using a 2D Gaussian Kernel (FWHM = 0.15 mm<sup>2</sup>). For Session 2, RS data and data obtained from the somatosensory and motor system experiments, the data were bandpass filtered between 0.01–0.3 Hz. The ultrafast data obtained during constant visual stimulation in Session 2 were bandpass filtered between 0.01–0.5 Hz.

**Retinotopic mapping analysis.** Retinotopic mapping analysis was performed using both conventional population receptive field (pRF) mapping<sup>103</sup> and micro-probing<sup>104</sup>. In brief, these methods model the visual field locations to which a population of neurons measured within a voxel respond to as a two-dimensional (2D) Gaussian, where the center corresponds to the pRF's position and the width to its size. In a previous study, we implemented these techniques to map the topographic structure of the rat visual pathway<sup>48</sup>.

#### Layer CF model analysis

**Layer definition.** Histological analysis determined the cortical depth ( $\mu$ m) corresponding to each cortical layer, as shown in Fig. 6D: LI (0–200  $\mu$ m), LII/III (200–600  $\mu$ m), LIV (600–900  $\mu$ m), LV (900–1450  $\mu$ m), and LVI (1450–2100  $\mu$ m). The cortical depth for each voxel was calculated by measuring the Euclidean distance from each cortical voxel to the brain surface, performed slice by slice. The brain surface was estimated by fitting a polynomial function to several manually selected points along the boundary of the brain surface. Voxels were then assigned to cortical layers based on their calculated cortical depth and the defined layer thickness.

**Layer CF model.** The ICF model predicts the neural activity of a recording site (voxel) in a target layer (e.g., layer IV of V2) based on the aggregate activity in a source layer or region (e.g., the entire LP or layer II of V1). This model extends the traditional CF approach as described by ref. 58. Each voxel's fMRI response is predicted using a 2D Gaussian CF model that spans across cortical layers. The key parameters of the CF model are its position and spatial spread (size) within the cortical layers. The layer specificity is derived from the high spatial resolution

data that we acquired, which allows not only to compute the CF size between brain areas but also between the layers of these areas. The core computation model is comprehensively explained in ref. 58. With a defined CF position and size, a predicted time-series is generated by weighting the CF model with the source BOLD time series. Optimal CF parameters are determined by minimizing the residual sum of squares between the predicted and actual time-series data. The risks of overfitting and underfitting are mitigated here through a coarse-to-fine estimation strategy. In this study, only CFs with a variance explained above 15% were retained, following criteria established in previous research<sup>86</sup>.

**Statistical analysis.** All statistical analyses were performed using MATLAB (version 2016b; Mathworks, Natick, Massachusetts, USA). Unless otherwise specified, after correction for multiple comparisons, a  $p$  value of 0.05 or less was considered statistically significant. Statistical comparisons of the CF properties (size and VE) were performed using ANOVA with post hoc analysis, Bonferroni corrected for multiple comparisons (brain area). Two-way  $t$ -tests were used to test whether the parabolic fits were significantly different from 0.

### Reporting summary

Further information on research design is available in the Nature Portfolio Reporting Summary linked to this article.

### Data availability

The raw data supporting the conclusions are available through (<https://doi.org/10.6084/m9.figshare.28736615>). Metadata is available via (<https://codeocean.com/capsule/0722166/tree/v1>). Source data are provided with this paper.

### Code availability

All the code used to generate all the Figures in this manuscript (including ICF calculation) can be accessed via OceanCode (<https://doi.org/10.24433/CO.4680084.v1>).

### References

1. Fişek, M. et al. Cortico-cortical feedback engages active dendrites in visual cortex. *Nature* **617**, 769–776 (2023).
2. Keller, A. J., Roth, M. M. & Scanziani, M. Feedback generates a second receptive field in neurons of the visual cortex. *Nature* **582**, 545–549 (2020).
3. Harris, J. A. et al. Hierarchical organization of cortical and thalamic connectivity. *Nature* **575**, 195–202 (2019).
4. Bolt, T. et al. A parsimonious description of global functional brain organization in three spatiotemporal patterns. *Nat. Neurosci.* **25**, 1093–1103 (2022).
5. Markov, N. T. & Kennedy, H. The importance of being hierarchical. *Curr. Opin. Neurobiol.* **23**, 187–194 (2013).
6. Aggarwal, A. et al. Visual evoked feedforward-feedback traveling waves organize neural activity across the cortical hierarchy in mice. *Nat. Commun.* **13**, 4754 (2022).
7. Yao, S. et al. A whole-brain monosynaptic input connectome to neuron classes in mouse visual cortex. *Nat. Neurosci.* **26**, 350–364 (2022).
8. Mantini, D. et al. Interspecies activity correlations reveal functional correspondence between monkey and human brain areas. *Nat. Methods* **9**, 277–282 (2012).
9. Pagani, M., Gutierrez-Barragan, D., de Guzman, A. E., Xu, T. & Gozzi, A. Mapping and comparing fMRI connectivity networks across species. *Commun. Biol.* **6**, 1–15 (2023).
10. Harris, K. D. & Mrsic-Flogel, T. D. Cortical connectivity and sensory coding. *Nature* **503**, 51–58 (2013).
11. Wang, R. et al. Distributed feedforward and feedback cortical processing supports human speech production. *Proc. Natl. Acad. Sci. USA* **120**, e2300255120 (2023).
12. Debes, S. R. & Dragoi, V. Suppressing feedback signals to visual cortex abolishes attentional modulation. *Science* **379**, 468–473 (2023).
13. Ferro, D., van Kempen, J., Boyd, M., Panzeri, S. & Thiele, A. Directed information exchange between cortical layers in macaque V1 and V4 and its modulation by selective attention. *Proc. Natl. Acad. Sci. USA* **118**, e2022097118 (2021).
14. Rao, R. P. & Ballard, D. H. Predictive coding in the visual cortex: a functional interpretation of some extra-classical receptive-field effects. *Nat. Neurosci.* **2**, 79–87 (1999).
15. Gilbert, C. D. & Li, W. Top-down influences on visual processing. *Nat. Rev. Neurosci.* **14**, 350–363 (2013).
16. Maeda, R. S., Gribble, P. L. & Pruszynski, J. A. Learning new feedforward motor commands based on feedback responses. *Curr. Biol.* **30**, 1941–1948.e3 (2020).
17. Lamme, V. A. Blindsight: the role of feedforward and feedback corticocortical connections. *Acta Psychol.* **107**, 209–228 (2001).
18. Roelfsema, P. R., van Ooyen, A. & Watanabe, T. Perceptual learning rules based on reinforcers and attention. *Trends Cogn. Sci.* **14**, 64–71 (2010).
19. Goldhacker, M., Rosengarth, K., Plank, T. & Greenlee, M. W. The effect of feedback on performance and brain activation during perceptual learning. *Vis. Res.* **99**, 99–110 (2014).
20. Aggarwal, A. et al. Glutamate indicators with improved activation kinetics and localization for imaging synaptic transmission. *Nat. Methods* **20**, 925–934 (2023).
21. Shen, S. et al. Distinct organization of two cortico-cortical feedback pathways. *Nat. Commun.* **13**, 6389 (2022).
22. Semedo, J. D. et al. Feedforward and feedback interactions between visual cortical areas use different population activity patterns. *Nat. Commun.* **13**, 1099 (2022).
23. van Kerkoerle, T. et al. Alpha and gamma oscillations characterize feedback and feedforward processing in monkey visual cortex. *Proc. Natl. Acad. Sci. USA* **111**, 14332–14341 (2014).
24. Chen, L., Cichy, R. M. & Kaiser, D. Alpha-frequency feedback to early visual cortex orchestrates coherent naturalistic vision. *Sci. Adv.* **9**, eadi2321 (2023).
25. Jensen, O., Bonnefond, M., Marshall, T. R. & Tiesinga, P. Oscillatory mechanisms of feedforward and feedback visual processing. *Trends Neurosci.* **38**, 192–194 (2015).
26. Menon, V. et al. Optogenetic stimulation of anterior insular cortex neurons in male rats reveals causal mechanisms underlying suppression of the default mode network by the salience network. *Nat. Commun.* **14**, 1–14 (2023).
27. Chao, T.-H. H. et al. Neuronal dynamics of the default mode network and anterior insular cortex: intrinsic properties and modulation by salient stimuli. *Sci. Adv.* **9**, eade5732 (2023).
28. Rocchi, F. et al. Increased fMRI connectivity upon chemogenetic inhibition of the mouse prefrontal cortex. *Nat. Commun.* **13**, 1–15 (2022).
29. Boulant, N. et al. In vivo imaging of the human brain with the Iseult 11.7-T MRI scanner. *Nat. Methods* **21**, 2013–2016 (2024).
30. Yu, X. et al. Sensory and optogenetically driven single-vessel fMRI. *Nat. Methods* **13**, 337–340 (2016).
31. Logothetis, N. K. What we can do and what we cannot do with fMRI. *Nature* **453**, 869–878 (2008).
32. Ma, Y. et al. Resting-state hemodynamics are spatiotemporally coupled to synchronized and symmetric neural activity in excitatory neurons. *Proc. Natl. Acad. Sci. USA* **113**, E8463–E8471 (2016).
33. Cerri, D. H. et al. Distinct neurochemical influences on fMRI response polarity in the striatum. *Nat. Commun.* **15**, 1–23 (2024).

34. Huber, L. et al. Layer-dependent functional connectivity methods. *Prog. Neurobiol.* **207**, 101835 (2021).
35. De Martino, F. et al. Cortical depth dependent functional responses in humans at 7T: improved specificity with 3D GRASE. *PLoS ONE* **8**, e60514 (2013).
36. Polimeni, J. R., Fischl, B., Greve, D. N. & Wald, L. L. Laminar analysis of 7T BOLD using an imposed spatial activation pattern in human V1. *Neuroimage* **52**, 1334–1346 (2010).
37. Muckli, L. et al. Contextual feedback to superficial layers of V1. *Curr. Biol.* **25**, 2690–2695 (2015).
38. Kok, P., Bains, L. J., van Mourik, T., Norris, D. G. & de Lange, F. P. Selective activation of the deep layers of the human primary visual cortex by top-down feedback. *Curr. Biol.* **26**, 371–376 (2016).
39. Lawrence, S. J. D., Norris, D. G. & Lange, de F. P.. Dissociable laminar profiles of concurrent bottom-up and top-down modulation in the human visual cortex. *eLife* **8**, e44422 (2019).
40. Carricarte, T. et al. Laminar dissociation of feedforward and feedback in high-level ventral visual cortex during imagery and perception. *iScience* **27**, 110229 (2024).
41. Felleman, D. J. & Van Essen, D. C. Distributed hierarchical processing in the primate cerebral cortex. *Cereb. Cortex* **1**, 1–47 (1991).
42. Lawrence, S. J., Norris, D. G. & de Lange, F. P. Dissociable laminar profiles of concurrent bottom-up and top-down modulation in the human visual cortex. *eLife* **8**, e44422 (2019).
43. Bergmann, J. et al. Cortical depth profiles in primary visual cortex for illusory and imaginary experiences. *Nat. Commun.* **15**, 1002 (2024).
44. Aitken, F. et al. Prior expectations evoke stimulus-specific activity in the deep layers of the primary visual cortex. *PLoS Biol.* **18**, e3001023 (2020).
45. Lawrence, S. J. D. et al. Laminar organization of working memory signals in human visual cortex. *Curr. Biol.* **28**, 3435–3440.e4 (2018).
46. van Kerkoerle, T., Self, M. W. & Roelfsema, P. R. Layer-specificity in the effects of attention and working memory on activity in primary visual cortex. *Nat. Commun.* **8**, 13804 (2017).
47. Drew, P. J., Mateo, C., Turner, K. L., Yu, X. & Kleinfeld, D. Ultra-slow oscillations in fMRI and resting-state connectivity: neuronal and vascular contributions and technical confounds. *Neuron* **107**, 782–804 (2020).
48. Carvalho, J., Fernandes, F. F. & Shemesh, N. Extensive topographic remapping and functional sharpening in the adult rat visual pathway upon first visual experience. *PLoS Biol.* **21**, e3002229 (2023).
49. Gil, R., Fernandes, F. F. & Shemesh, N. Neuroplasticity-driven timing modulations revealed by ultrafast functional magnetic resonance imaging. *NeuroImage* **225**, 117446 (2021).
50. Cabral, J., Fernandes, F. F. & Shemesh, N. Intrinsic macroscale oscillatory modes driving long range functional connectivity in female rat brains detected by ultrafast fMRI. *Nat. Commun.* **14**, 375 (2023).
51. Jung, W. B., Im, G. H., Jiang, H. & Kim, S.-G. Early fMRI responses to somatosensory and optogenetic stimulation reflect neural information flow. *Proc. Natl. Acad. Sci. USA* **118**, e2023265118 (2021).
52. Choi, S. et al. Laminar-specific functional connectivity mapping with multi-slice line-scanning fMRI. *Cereb. Cortex* **32**, 4492–4501 (2022).
53. Yu, X., Qian, C., Chen, D.-Y., Dodd, S. J. & Koretsky, A. P. Deciphering laminar-specific neural inputs with line-scanning fMRI. *Nat. Methods* **11**, 55–58 (2014).
54. Raimondo, L. et al. A line through the brain: implementation of human line-scanning at 7T for ultra-high spatiotemporal resolution fMRI. *J. Cereb. Blood Flow. Metab.* **41**, 2831–2843 (2021).
55. Gil, R., Valente, M. & Shemesh, N. Rat superior colliculus encodes the transition between static and dynamic vision modes. *Nat. Commun.* **15**, 849 (2024).
56. Gutierrez-Barragan, D. et al. Unique spatiotemporal fMRI dynamics in the awake mouse brain. *Curr. Biol.* **32**, 631–644.e6 (2022).
57. Shi, L. et al. Global spatiotemporal synchronizing structures of spontaneous neural activities in different cell types. *Nat. Commun.* **15**, 1–17 (2024).
58. Haak, K. V. et al. Connective field modeling. *Neuroimage* **66**, 376–384 (2013).
59. Invernizzi, A., Haak, K. V., Carvalho, J. C., Renken, R. J. & Cornelissen, F. W. Bayesian connective field modeling using a Markov Chain Monte Carlo approach. *Neuroimage* **264**, 119688 (2022).
60. Wandell, B. A. & Winawer, J. Computational neuroimaging and population receptive fields. *Trends Cogn. Sci.* **19**, 349–357 (2015).
61. Gravel, N. et al. Cortical connective field estimates from resting state fMRI activity. *Front. Neurosci.* **8**, 339 (2014).
62. Knapen, T. Topographic connectivity reveals task-dependent retinotopic processing throughout the human brain. *Proc. Natl. Acad. Sci. USA* **118**, e2017032118 (2021).
63. de Best, P. B., Abulafia, R., McKyton, A. & Levin, N. Convergence along the visual hierarchy is altered in posterior cortical atrophy. *Invest. Ophthalmol. Vis. Sci.* **61**, 8 (2020).
64. Choi, S., Chen, Y., Zeng, H., Biswal, B. & Yu, X. Identifying the distinct spectral dynamics of laminar-specific interhemispheric connectivity with bilateral line-scanning fMRI. *J. Cereb. Blood Flow. Metab.* **43**, 1115–1129 (2023).
65. Wang, L., Saalmann, Y. B., Pinsk, M. A., Arcaro, M. J. & Kastner, S. Electrophysiological low-frequency coherence and cross-frequency coupling contribute to BOLD connectivity. *Neuron* **76**, 1010–1020 (2012).
66. Ringach, D. L. Spontaneous and driven cortical activity: implications for computation. *Curr. Opin. Neurobiol.* **19**, 439–444 (2009).
67. Zhang, Y. & Zhang, X. Portrait of visual cortical circuits for generating neural oscillation dynamics. *Cogn. Neurodyn.* **15**, 3–16 (2021).
68. Ji, W. et al. Modularity in the organization of mouse primary visual cortex. *Neuron* **87**, 632–643 (2015).
69. Briggs, F. Organizing principles of cortical layer 6. *Front. Neural Circuits* **4**, 3 (2010).
70. Markov, N. T. et al. Anatomy of hierarchy: feedforward and feedback pathways in macaque visual cortex. *J. Comp. Neurol.* **522**, 225–259 (2014).
71. Bastos, A. M. et al. Canonical microcircuits for predictive coding. *Neuron* **76**, 695–711 (2012).
72. Douglas, R. J. & Martin, K. A. C. Neuronal circuits of the neocortex. *Annu. Rev. Neurosci.* **27**, 419–451 (2004).
73. Jia, X. et al. Multi-regional module-based signal transmission in mouse visual cortex. *Neuron* **110**, 1585–1598.e9 (2022).
74. Tohmi, M., Meguro, R., Tsukano, H., Hishida, R. & Shibuki, K. The extrageniculate visual pathway generates distinct response properties in the higher visual areas of mice. *Curr. Biol.* **24**, 587–597 (2014).
75. Bock, A. S. et al. Resting-state retinotopic organization in the absence of retinal input and visual experience. *J. Neurosci.* **35**, 12366–12382 (2015).
76. Coleman, J. & Clerici, W. J. Extrastriate projections from thalamus to posterior occipital-temporal cortex in rat. *Brain Res.* **194**, 205–209 (1980).
77. Warner, C. E. et al. Preservation of vision by the pulvinar following early-life primary visual cortex lesions. *Curr. Biol.* **25**, 424–434 (2015).
78. Atapour, N., Worthy, K. H. & Rosa, M. G. P. Remodeling of lateral geniculate nucleus projections to extrastriate area MT following long-term lesions of striate cortex. *Proc. Natl. Acad. Sci. USA* **119**, e2117137119 (2022).

79. Rima, S. & Schmid, M. C. V1-bypassing thalamo-cortical visual circuits in blindsight and developmental dyslexia. *Curr. Opin. Physiol.* **16**, 14–20 (2020).
80. Yu, X. et al. Thalamocortical inputs show post-critical-period plasticity. *Neuron* **74**, 731–742 (2012).
81. Keck, T. et al. Massive restructuring of neuronal circuits during functional reorganization of adult visual cortex. *Nat. Neurosci.* **11**, 1162–1167 (2008).
82. Mitra, A. *Spatio-Temporal Principles of Infra-Slow Brain Activity* (2019).
83. Mitra, A. et al. Spontaneous infra-slow brain activity has unique spatiotemporal dynamics and laminar structure. *Neuron* **98**, 297–305.e6 (2018).
84. Ooi, L. Q. R. et al. Longer scans boost prediction and cut costs in brain-wide association studies. *Nature* **644**, 731–740 (2025).
85. Lin, F.-H. et al. Increasing fMRI sampling rate improves Granger causality estimates. *PLoS ONE* **9**, e100319 (2014).
86. Chuang, K.-H., Li, Z., Huang, H. H., Khorasani Gerdekoohi, S. & Athwal, D. Hemodynamic transient and functional connectivity follow structural connectivity and cell type over the brain hierarchy. *Proc. Natl. Acad. Sci. USA* **120**, e2202435120 (2023).
87. Thompson, G. J., Pan, W.-J., Magnuson, M. E., Jaeger, D. & Keilholz, S. D. Quasi-periodic patterns (QPP): large-scale dynamics in resting state fMRI that correlate with local infraslow electrical activity. *Neuroimage* **84**, 1018–1031 (2014).
88. Barth, M., Breuer, F., Koopmans, P. J., Norris, D. G. & Poser, B. A. Simultaneous multislice (SMS) imaging techniques. *Magn. Reson. Med.* **75**, 63–81 (2016).
89. Reynaud, O., da Silva, A. R., Gruetter, R. & Jolescu, I. O. Multi-slice passband bSSFP for human and rodent fMRI at ultra-high field. *J. Magn. Reson.* **305**, 31–40 (2019).
90. Vergara, V. M., Salman, M., Abrol, A., Espinoza, F. A. & Calhoun, V. D. Determining the number of states in dynamic functional connectivity using cluster validity indexes. *J. Neurosci. Methods* **337**, 108651 (2020).
91. Frühholz, S., Trost, W., Grandjean, D. & Belin, P. Neural oscillations in human auditory cortex revealed by fast fMRI during auditory perception. *Neuroimage* **207**, 116401 (2020).
92. Lewis, L. D., Setsompop, K., Rosen, B. R. & Polimeni, J. R. Fast fMRI can detect oscillatory neural activity in humans. *Proc. Natl. Acad. Sci. USA* **113**, E6679–E6685 (2016).
93. Cordes, D. et al. Mapping functionally related regions of brain with functional connectivity MR imaging. *Am. J. Neuroradiol.* **21**, 1636–1644 (2000).
94. Pradier, B. et al. Combined resting state-fMRI and calcium recordings show stable brain states for task-induced fMRI in mice under combined ISO/MED anesthesia. *Neuroimage* **245**, 118626 (2021).
95. You, T., Im, G. H. & Kim, S.-G. Characterization of brain-wide somatosensory BOLD fMRI in mice under dexmedetomidine/isoflurane and ketamine/xylazine. *Sci. Rep.* **11**, 13110 (2021).
96. Tian, P. et al. Cortical depth-specific microvascular dilation underlies laminar differences in blood oxygenation level-dependent functional MRI signal. *Proc. Natl. Acad. Sci. USA* **107**, 15246–15251 (2010).
97. Lee, H.-L., Li, Z., Coulson, E. J. & Chuang, K.-H. Ultrafast fMRI of the rodent brain using simultaneous multi-slice EPI. *Neuroimage* **195**, 48–58 (2019).
98. Tsurugizawa, T., Takahashi, Y. & Kato, F. Distinct effects of isoflurane on basal BOLD signals in tissue/vascular microstructures in rats. *Sci. Rep.* **6**, 38977 (2016).
99. Zhu, W., Zhang, G., Zhu, X.-H. & Chen, W. A robust approach for analyzing and mapping hierarchical brain connectome towards laminar-specific neural networks. *Imaging Neurosci.* **3**, imag\_a\_00543 (2025).
100. Fernandes, F. F., Olesen, J. L., Jespersen, S. N. & Shemesh, N. MP-PCA denoising of fMRI time-series data can lead to artificial activation ‘spreading’. *Neuroimage* **273**, 120118 (2023).
101. Roche, A. A four-dimensional registration algorithm with application to joint correction of motion and slice timing in fMRI. *IEEE Trans. Med. Imaging* **30**, 1546–1554 (2011).
102. Barrière, D. A. et al. The SIGMA rat brain templates and atlases for multimodal MRI data analysis and visualization. *Nat. Commun.* **10**, 5699 (2019).
103. Dumoulin, S. O. & Wandell, B. A. Population receptive field estimates in human visual cortex. *Neuroimage* **39**, 647–660 (2008).
104. Carvalho, J. et al. Micro-probing enables fine-grained mapping of neuronal populations using fMRI. *Neuroimage* **209**, 116423 (2020).

## Acknowledgements

This study was funded by the European Research Council (ERC) (agreement No. 679058), by the European Union’s Horizon 2020 research and innovation programme under the Marie Skłodowska-Curie grant agreement No. 101032056, and by the Fundação para a Ciência e Tecnologia (FCT) exploratory Grant (No. 2022.07889.PTDC). K.H. gratefully acknowledges funding from the Dutch Research Council (NWO; Vidi grant no. 09150171910043). M.V. thanks FCT for a PhD fellowship PD/BD/141560/2018. The funding organizations had no role in the design, conduct, analysis, or publication of this research. The authors acknowledge the vivarium of the Champalimaud Centre for the Unknown, a facility of CONGENTO, which is a research infrastructure co-financed by Lisboa Regional Operational Programme (Lisboa 2020), under the PORTUGAL 2020 Partnership Agreement through the European Regional Development Fund (ERDF) and Fundação para a Ciência e Tecnologia (Portugal), project LISBOA-01-0145-FEDER-022170. NS is generously supported by the Center for New Scientists and the Many Igel Centre for Biomedical Engineering and Signal Processing at the Weizmann Institute of Science.

## Author contributions

J.C., N.S., and K.H. designed the project and the necessary experiments, and N.S. oversaw the implementation of the project. J.C. and F.F. acquired the data; M.V. acquired and performed the lesions and histology analysis. J.C. analyzed the data. All authors wrote the paper. All authors discussed the results and implications and commented on the manuscript at all stages.

## Competing interests

The authors declare the following competing interests: N.S. serves on the scientific advisory board of Bruker Biospin. The other authors declare no competing interests.

## Additional information

**Supplementary information** The online version contains supplementary material available at <https://doi.org/10.1038/s41467-026-71506-9>.

**Correspondence** and requests for materials should be addressed to Joana Carvalho or Noam Shemesh.

**Peer review information** *Nature Communications* thanks Yen-Yu Shih, who co-reviewed with Samuel BoothWei Chen and Xin Yu for their contribution to the peer review of this work. A peer review file is available.

**Reprints and permissions information** is available at <http://www.nature.com/reprints>

**Publisher’s note** Springer Nature remains neutral with regard to jurisdictional claims in published maps and institutional affiliations.

**Open Access** This article is licensed under a Creative Commons Attribution-NonCommercial-NoDerivatives 4.0 International License, which permits any non-commercial use, sharing, distribution and reproduction in any medium or format, as long as you give appropriate credit to the original author(s) and the source, provide a link to the Creative Commons licence, and indicate if you modified the licensed material. You do not have permission under this licence to share adapted material derived from this article or parts of it. The images or other third party material in this article are included in the article's Creative Commons licence, unless indicated otherwise in a credit line to the material. If material is not included in the article's Creative Commons licence and your intended use is not permitted by statutory regulation or exceeds the permitted use, you will need to obtain permission directly from the copyright holder. To view a copy of this licence, visit <http://creativecommons.org/licenses/by-nc-nd/4.0/>.

© The Author(s) 2026